50th AIAA Aerospace Sciences Meeting including the New Horizons Forum and Aerospace Exposition
09 - 12 January 2012, Nashville, Tennessee
AIAA 2012-0541

Transverse Waves in Simulated Liquid Rocket Engines with Variable Headwall Injection

Charles T. Haddad* and Joseph Majdalani†
University of Tennessee Space Institute, Tullahoma, TN 37388

In this study, the transverse vorticoacoustic wave in a circular cylinder is characterized for a variable velocity profile at the injector faceplate. This particular configuration mimics the conditions leading to the onset of traveling radial and tangential waves in a simple liquid rocket engine (LRE). To capture the unsteady behavior in this physical setting, we consider a short thrust chamber with an injecting headwall and combine the benefits of three techniques: regular perturbations, Helmholtz decomposition, and boundary layer theory. First, regular perturbations are leveraged to linearize the equations of motion and, in the process, help to identify the unsteady interaction equations. Second, a Helmholtz decomposition of the first-order disturbance equations gives rise to a compressible, inviscid, and acoustic set that is responsible for driving the unsteady motion. This is accomplished in conjunction with an essentially incompressible, viscous, and vortical set that materializes by virtue of coupling with the acoustic wave at the boundaries. After recovering the acoustic mode from the resulting wave equation, the last step is to solve for the vortical mode by applying boundary layer theory and a judicious expansion of the rotational set with respect to a small viscous parameter, δ. After some effort, an explicit formulation for variable headwall injection is obtained and validated by means of a limiting process verification that is based on two previously investigated cases, the uniform and bell-shaped injection profiles. The solution is then illustrated using two new configurations corresponding to laminar and turbulent profiles. In the process of comparing the four representative cases, the characteristics of the vorticoacoustic wave, including its penetration depth, spatial wavelength, and overshoot factor, are systematically explored and discussed. Most characteristics are found to depend on the penetration and Strouhal numbers along with the distance from the centerline. Along the axis of the chamber, the waves attributed to different injection profiles behave similarly to the extent that behavioral deviations among them increase as the sidewall is approached. This work also accounts for the presence of a downstream boundary that stands to produce left-traveling reflections whose pairing with the right-traveling waves promotes the establishment of a standing wave environment. The combined waves are formulated analytically and shown to be appreciable in view of their amplitudes that twice exceed those associated with traveling waves.

Nomenclature

a_0	=	speed of sound of incoming flow, $(\gamma R T_0)^{1/2}$
$\boldsymbol{e}_r, \boldsymbol{e}_\theta, \boldsymbol{e}_z$	=	unit vectors in $r, \theta,$ and z directions
f_{mn}	=	transverse frequency, $\omega_{mn}/(2\pi) = a_0 k_{mn}/(2\pi R)$
L, R	=	chamber length and radius, respectively
M_b	=	average blowing/burning Mach number at headwall, U_b / a_0
OF	=	overshoot factor
p	=	pressure
Pr	=	Prandtl number, ratio of kinematic viscosity and thermal diffusivity

*Graduate Research Assistant, Department of Mechanical, Aerospace and Biomedical Engineering. Member AIAA.
†H. H. Arnold Chair of Excellence in Advanced Propulsion, Department of Mechanical, Aerospace and Biomedical Engineering. Associate Fellow AIAA. Fellow ASME.

Copyright © 2012 by C. T. Haddad and J. Majdalani. Published by the American Institute of Aeronautics and Astronautics, Inc., with permission.

r, θ, z = radial, tangential, and axial coordinates
Re_a = acoustic Reynolds number, $a_0 R / \nu_0$
Re_b = blowing (or wall injection) Reynolds number, $U_b R / \nu_0$
S = Strouhal number, $k_{mn} / M_b = 2\pi f_{mn} R / U_b$
S_p = penetration number, $U_b^3 / (\omega_{mn}^2 \nu_0 R) = U_b^3 / (4\pi^2 f_{mn}^2 \nu_0 R)$
t = time
T = temperature
$\boldsymbol{u}$ = total velocity vector
$U_b(r)$ = headwall velocity profile
$\boldsymbol{U}$ = mean flow velocity vector
V_w = propagation velocity of vortical waves in the axial direction
y_p = penetration depth of rotational elements in the y direction
z_p = penetration depth of rotational elements in the z direction
z_{OS} = locus of unsteady velocity overshoot

Greek
δ = viscous parameter, $1/\sqrt{Re_a}$
δ_d = dilatational parameter, $\delta(\eta_0/\mu_0 + 4/3)^{1/2}$
ε = wave amplitude
γ = ratio of specific heats
η = second coefficient of viscosity, $\mu_{\mathrm{bulk}} - 2\mu/3$
λ_w = spatial wave length
μ = dynamic viscosity
μ_{bulk} = bulk viscosity
ν = kinematic viscosity, μ/ρ
ρ = density
$\boldsymbol{\Omega}, \boldsymbol{\omega}$ = mean or unsteady vorticity
ω_{mn} = circular frequency, $2\pi f_{mn} = a_0 k_{mn} / R$

Subscripts
0 = mean chamber property or reference value
r, θ, z = radial, tangential, and axial directions

Superscripts
$*$ = dimensional variables
$'$ = unsteady flow variable
(0) = leading-order variable
(1) = first-order variable

I. Introduction

THIS study aims at investigating the mathematical forms of the vorticoacoustic waves that can be engendered inside a simulated liquid rocket engine (LRE) with a strongly injecting headwall. The rotational gaseous motion that arises in such an environment may be described by a set of four coupled partial differential equations (PDEs) representing continuity and momentum conservation in the context of a fluid oscillating in a relatively short cylindrical chamber with a permeable headwall.[1,2] The formulation to be developed here will therefore seek to accommodate a multitude of axisymmetric mean flow velocities that may be envisioned along conventional injector faceplates. These will be seen to influence the chamber's vorticoacoustic wave oscillations. In the process, the nonlinear interactions that develop between the bulk and unsteady gaseous motions will be explored and shown to produce rich structures that we plan to characterize assuming a non-reactive cold flow environment of a simulated LRE chamber.

Thus far, a variety of exact and asymptotic solutions have been developed using mathematical models of the vorticoacoustic field arising in simulated solid rocket motors (SRMs) with either cylindrical[3,4] or planar configurations.[5-8] In SRMs, however, the unsteady motion remains primarily dominated by longitudinal oscillations

due, in large part, to the presence of distributed sidewall mass addition and high chamber aspect ratios. In sharp contrast, the headwall-driven gaseous injection and the typically low aspect ratios associated with LRE thrust chambers lead to a predominantly transverse wave environment.[9-11] It is well known, for example, that in most LREs, large pressure oscillations appear in a plane that is normal to the chamber axis, thus leading to transverse mode instabilities whose reported frequencies closely match the modes predicted by linear chamber acoustics.[12,13]

In recent work on the subject, Fischbach, Flandro and Majdalani[1] revisit the transverse wave problem in a simulated LRE with uniform headwall injection. However, their chief objective remains focused on understanding the mechanism of acoustic streaming rather than the vorticoacoustic wave character itself. In a follow-up study, Haddad and Majdalani[2] introduce a higher-order solution of the rotationally traveling wave in a similarly configured LRE. At the outset, formulations are produced for both uniform and bell-shaped injection profiles, with the latter constituting a more realistic representation of the mean flow. Both studies feature a circular-port configuration that may be viewed as analogous to the idealized SRM problem with the main difference being in the SRM sidewall exchanging roles with the LRE headwall. In this article, the procedure developed for specific injection patterns will be generalized to encompass an arbitrary mean flow profile.[14] Moreover, both traveling and standing wave forms associated with such motions will be constructed asymptotically and characterized.

To set the stage, the flowfield developed inside a right-cylindrical chamber having a low aspect ratio and a normally injecting headwall will be considered. According to our idealization, the mean gaseous motion is induced by a variable axisymmetric injection pattern. Due to unavoidable flow fluctuations within the chamber, small-amplitude acoustic waves are promptly promoted and sustained. The resulting self-excited waves give rise to a complex flow motion that we wish to analyze. Based on the small-perturbation technique introduced by Chu and Kovásznay,[15] the conservation equations are recast into two sets of relations, one controlling the mean flow behavior, and the other describing the oscillatory motion. The first-order oscillatory set is then decomposed into a pair of acoustic and vortical fields using the Helmholtz decomposition concept.[6] These classical techniques are therefore leveraged to derive an improved asymptotic approximation of the oscillatory motion in a circular chamber in general, and a simulated LRE in particular. Then using a systematic application of boundary layer theory, a crisp mathematical formulation is achieved for the right-traveling vorticoacoustic wave motion associated with a variable headwall injection profile. The resulting solution will be shown to be sufficiently general to permit the recovery of previous approximations[1,2] as special cases. Lastly, the effect of a downstream boundary on producing reflected waves will be examined along with the solution of the resulting standing wave structure.

II. Formulation

A. Geometry

This work is connected with the stability analysis and wave dynamics within LRE thrust chambers. In this vein, we consider a circular-port chamber in which rapid combustion has already occurred to the extent of justifying the use of a non-reactive gaseous mixture as the working fluid. We proceed by showing in Fig. 1 a schematic of the idealized thrust chamber which is simulated as a right-cylindrical chamber that extends vertically from the center axis at $r^* = 0$ to the sidewall at $r^* = R$. Horizontally, the domain extends from $z^* = 0$ to L, where the headwall

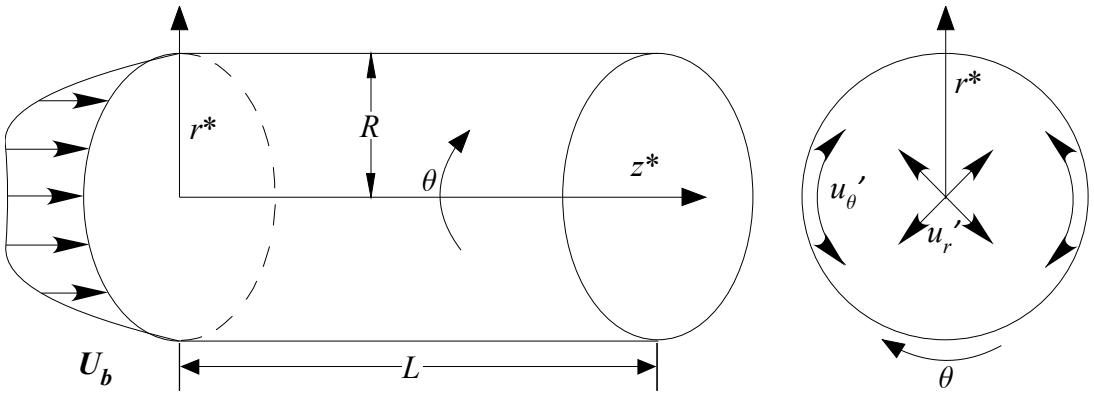

Figure 1. Chamber geometry and coordinate system showing a generally axisymmetric injection profile. Included is a front view depicting the coupled radial and tangential wave motions that constitute the transverse modes.

may be viewed as a porous surface across which flow may enter at a velocity $U_b(r)$. In this framework, θ defines the azimuthal coordinate and the transverse direction of unsteady velocity disturbances, u'_θ and u'_r, denote the tangential and radial oscillations, respectively. Given that this study is chiefly concerned with a simulated LRE, the aspect ratio of the enclosure at hand is taken to be low, specifically less than or equal to unity, $L/R \le 1$.

B. Normalized System of Equations

For a solution that may be universally applied to different injection profiles, reliance on a judicious choice of dimensionless variables seems essential. Generally speaking, normalized results lead to more concise representations while offering the benefit of reverting back to the original, dimensional variables quite straightforwardly. In this vein, we proceed by normalizing the flow variables according to

$$\begin{cases} p = p^* / P_0 & \boldsymbol{u} = \boldsymbol{u}^* / a_0 & r = r^* / R & T = T^* / T_0 \\ \rho = \rho^* / \rho_0 & t = t^* / (R / a_0) & z = z^* / R & \boldsymbol{\omega} = \boldsymbol{\omega}^* / (a_0 / R) \end{cases} \tag{1}$$

where reference properties are defined in the Nomenclature. The normalized equations for a viscous compressible fluid, with no body forces acting on it, may be expressed as

Mass:
$$\frac{\partial \rho}{\partial t} + \nabla \cdot (\rho \boldsymbol{u}) = 0 \tag{2}$$

Momentum:
$$\rho \left[\frac{\partial \boldsymbol{u}}{\partial t} + \frac{1}{2} \nabla (\boldsymbol{u} \cdot \boldsymbol{u}) - \boldsymbol{u} \times \nabla \times \boldsymbol{u} \right] = -\frac{1}{\gamma} \nabla p - \delta^2 \nabla \times (\nabla \times \boldsymbol{u}) + \delta_d^2 \nabla (\nabla \cdot \boldsymbol{u}) \tag{3}$$

Energy:
$$\rho \left(\frac{\partial T}{\partial t} + \boldsymbol{u} \cdot \nabla T \right) = \frac{\gamma - 1}{\gamma} \left(\frac{\partial p}{\partial t} + \boldsymbol{u} \cdot \nabla p \right) + \frac{\delta^2}{Pr_0} \nabla^2 T \tag{4}$$

State:
$$p = \rho T \tag{5}$$

where Pr and γ refer to the Prandtl number and the ratio of specific heats, respectively. The viscous parameters δ and δ_d are given by

$$\delta = \sqrt{\frac{\nu_0}{a_0 R}} = \sqrt{\frac{1}{Re_a}}; \quad \delta_d = \delta \sqrt{\frac{\eta_0}{\mu_0} + \frac{4}{3}} \tag{6}$$

It may be interesting to remark that the bulk viscosity, also known as the dilatational viscosity η, is taken here at the reference conditions as η_0. This parameter stems from the viscous shear term associated with the volumetric-rate-of-strain, and is routinely set equal to zero when the fluid is incompressible, as predicated by the Stokes hypothesis. Moreover, in the case of a rapid adiabatic disturbance in which friction may be ignored (i.e., in the case of an inviscid, fast traveling, acoustic wave disturbance), the isentropic relation may be used instead of the energy equation. When put in dimensionless form, the pressure-density relation becomes

$$p = \rho^\gamma \tag{7}$$

C. Unsteady Disturbance Equations

After normalization, the first stage in solving Eqs. (2)–(5) is to separate the normalized flow variables in terms of a mean flow and an oscillatory component. This strategy, first introduced and vetted by Chu and Kovásznay,[15] has been ubiquitously employed in the literature.[16,17] Known examples showcasing its importance include the reduction of the velocity-potential equation into a simpler, more manageable form and the derivation of the 1-D acoustic wave equation.[18-20] The normalized flow variables can hence be decomposed using

$$\boldsymbol{u} = M_b \boldsymbol{U} + \boldsymbol{u}'; \quad \boldsymbol{\omega} = \bar{\boldsymbol{\Omega}} + \boldsymbol{\omega}'; \quad p = 1 + p'; \quad \rho = 1 + \rho'; \quad T = 1 + T' \tag{8}$$

The instantaneous variables in Eq. (8) may be substituted into Eqs. (2)–(5), thus leading to two sets of equations for the steady and unsteady fields.[5,21] The next step consists of expanding all unsteady variables in terms of the primary perturbation parameter, ε. In the process, each fluctuation q' may be written as

$$q' = \varepsilon q^{(1)} + \varepsilon^2 q^{(2)} + \varepsilon^3 q^{(3)} + \mathcal{O}(\varepsilon^4) \tag{9}$$

Here q alludes to a generic flow variable, and ε denotes the ratio of the superimposed oscillatory pressure amplitude to the traditionally larger mean chamber pressure. The expanded quantities may be later separated and rearranged by orders of the perturbation parameter. These sets can be solved sequentially for every order of ε, except for the leading-order set that corresponds to the mean flow profile. In this study, the steady-state motion is

determined by the externally prescribed headwall injection pattern. As such, the forthcoming analysis focuses on the first-order interaction equations that describe the motion of the unsteady field. These are given by

$$\frac{\partial \rho^{(1)}}{\partial t} = -\nabla \cdot \boldsymbol{u}^{(1)} - M_b \nabla \cdot \left[\rho^{(1)} \boldsymbol{U} \right] \tag{10}$$

$$\frac{\partial \boldsymbol{u}^{(1)}}{\partial t} = -\frac{1}{\gamma} \nabla p^{(1)} - M_b \left\{ \nabla \left[\boldsymbol{U} \cdot \boldsymbol{u}^{(1)} \right] - \boldsymbol{U} \times \boldsymbol{\omega}^{(1)} - \boldsymbol{u}^{(1)} \times \bar{\boldsymbol{\Omega}} \right\} - \delta^2 \nabla \times \boldsymbol{\omega}^{(1)} + \delta_d^2 \nabla \left[\nabla \cdot \boldsymbol{u}^{(1)} \right] \tag{11}$$

$$\frac{\partial T^{(1)}}{\partial t} = -M_b \boldsymbol{U} \cdot \nabla T^{(1)} + \frac{\gamma - 1}{\gamma} \left[\frac{\partial p^{(1)}}{\partial t} + M_b \boldsymbol{U} \cdot \nabla p^{(1)} \right] + \frac{\delta^2}{Pr} \nabla^2 T^{(1)} \tag{12}$$

$$p^{(1)} = T^{(1)} + \rho^{(1)} \tag{13}$$

D. Headwall Injection Pattern

As one may infer from Eqs. (10)–(13), the mean flow ($\boldsymbol{U}$) exhibits a strong influence on the oscillatory behavior in the chamber by controlling the bulk gaseous transport within the chamber. In practice, the inflow of propellants across traditional faceplates remains susceptible to the number, location, orientation, and size of headwall injectors along with their corresponding inlet velocities. Nonetheless, despite the complex injection patterns that may be present, a streamtube motion quickly develops, especially for conventional thrust chambers.[22] Bearing these factors in mind, our analysis will devote itself to simple and axisymmetric representations of the incoming stream.

Our main procedure unfolds as follows: To start, the general solution is derived and then examined for four dissimilar yet axisymmetric injection configurations. The first corresponds to a uniform, top-hat, plug flow along the chamber length. The second implements a bell-shaped, half-cosine that has been in some cases named after Berman.[23] The latter has been frequently used in theoretical studies of propulsive systems with wall injection. Examples include, but are not limited to, those by Culick,[24] Brown *et al.*,[25] Proudman,[26] Beddini,[27] Chedevergne, Casalis and Féraille,[28] Griffond and Casalis,[29] Saad and Majdalani[30] and Majdalani.[31] The third and fourth injection profiles are common to the fluid dynamics community and represent laminar and turbulent velocity profiles in circular tubes.[32] The four representative test cases may be expressed in non-dimensional form using

Uniform profile: $$\boldsymbol{U} = (0)\boldsymbol{e}_r + (0)\boldsymbol{e}_\theta + (1)\boldsymbol{e}_z \tag{14}$$

Berman (bell-shaped) profile: $$\boldsymbol{U} = (0)\boldsymbol{e}_r + (0)\boldsymbol{e}_\theta + \cos(\tfrac{1}{2}\pi r^2)\boldsymbol{e}_z \tag{15}$$

Laminar profile: $$\boldsymbol{U} = (0)\boldsymbol{e}_r + (0)\boldsymbol{e}_\theta + (1-r^2)\boldsymbol{e}_z \tag{16}$$

Turbulent profile: $$\boldsymbol{U} = (0)\boldsymbol{e}_r + (0)\boldsymbol{e}_\theta + (1-r)^{1/7}\boldsymbol{e}_z \tag{17}$$

where all velocities are normalized with respect to the centerline speed at $z = 0$.

In the above, the mean velocity vector ($\boldsymbol{U}$) stands for the arbitrary injection profile. In all four test cases, $\boldsymbol{U}$ appears as a sole function of the normalized radius, with no radial or tangential components. These assumptions enable us to combine Eqs. (14)–(17) into one generic form, namely

$$\boldsymbol{U} = (0)\boldsymbol{e}_r + (0)\boldsymbol{e}_\theta + F(r)\boldsymbol{e}_z \tag{18}$$

where $F = F(r)$ corresponds to 1, $\cos(\tfrac{1}{2}\pi r^2)$, $1-r^2$, and $(1-r)^{1/7}$ for the uniform, bell-shaped, laminar, and turbulent profiles, respectively. It may be worth mentioning that for $0 \le r \le 1$, $F \ge 0$. This observation will be helpful to recall while formulating the upcoming vortical solution.

E. Flowfield Decomposition

In comparable studies leading to analytical solutions of wave motions, first-order fluctuations are invariably separated into either an acoustic or a vortical field.[4,33] Because the acoustic part remains inviscid, it proves incapable of satisfying the velocity adherence condition at solid boundaries. Both physically and mathematically, a correction is required, namely, in the form of a vortical wave. Using a circumflex to denote the pressure-driven potential part, and a tilde for the boundary-driven vortical component, the unsteady flow variables may be once more partitioned into:

$$\boldsymbol{u}^{(1)} = \hat{\boldsymbol{u}} + \tilde{\boldsymbol{u}}; \quad \boldsymbol{\omega}^{(1)} = \hat{\boldsymbol{\omega}} + \tilde{\boldsymbol{\omega}}; \quad p^{(1)} = \hat{p} + \tilde{p}; \quad \rho^{(1)} = \hat{\rho} + \tilde{\rho}; \quad T^{(1)} = \hat{T} + \tilde{T} \tag{19}$$

Substituting Eq. (19) into Eqs. (10)–(13) yields two independent sets of equations that remain coupled by virtue of the no-slip requirement at the headwall.[6] These are:

Table 1. Boundary conditions for the acoustic and vortical fields

	Boundary		
	$r=1$	$z=0$	$z=L/R$
Acoustic field	$\mathbf{n}\cdot\nabla\hat{p}=0$	$\mathbf{n}\cdot\nabla\hat{p}=0$	$\mathbf{n}\cdot\nabla\hat{p}=0$
Vortical field	no condition imposed	$u_r'=u_\theta'=u_z'=0$	bounded

Acoustic set:

$$\frac{\partial\hat{\rho}}{\partial t}=-\nabla\cdot\hat{\boldsymbol{u}}-M_b\boldsymbol{U}\nabla\cdot\hat{\rho} \tag{20}$$

$$\frac{\partial\hat{\boldsymbol{u}}}{\partial t}=-\frac{1}{\gamma}\nabla\hat{p}-M_b\left[\nabla\left(\boldsymbol{U}\cdot\hat{\boldsymbol{u}}\right)-\hat{\boldsymbol{u}}\times\bar{\boldsymbol{\Omega}}\right] \tag{21}$$

$$\frac{\partial\hat{T}}{\partial t}=-M_b\boldsymbol{U}\cdot\nabla\hat{T}+\frac{\gamma-1}{\gamma}\left(\frac{\partial\hat{p}}{\partial t}+M_b\boldsymbol{U}\cdot\nabla\hat{p}\right) \tag{22}$$

$$\hat{p}=\hat{T}+\hat{\rho} \tag{23}$$

$$\hat{p}=\gamma\hat{\rho} \tag{24}$$

Vortical set:

$$\nabla\cdot\tilde{\boldsymbol{u}}=0 \tag{25}$$

$$\frac{\partial\tilde{\boldsymbol{u}}}{\partial t}=-\frac{1}{\gamma}\nabla\tilde{p}-M_b\left[\nabla\left(\boldsymbol{U}\cdot\tilde{\boldsymbol{u}}\right)-\boldsymbol{U}\times\tilde{\boldsymbol{\omega}}-\tilde{\boldsymbol{u}}\times\bar{\boldsymbol{\Omega}}\right]-\delta^2\nabla\times\tilde{\boldsymbol{\omega}}+\delta_d^2\nabla\left(\nabla\cdot\tilde{\boldsymbol{u}}\right) \tag{26}$$

$$\frac{\partial\tilde{T}}{\partial t}=-M_b\boldsymbol{U}\cdot\nabla\tilde{T}+\frac{\gamma-1}{\gamma}\left(\frac{\partial\tilde{p}}{\partial t}+M_b\boldsymbol{U}\cdot\nabla\tilde{p}\right)+\frac{\delta^2}{Pr}\nabla^2\tilde{T} \tag{27}$$

$$\tilde{p}=\tilde{T}+\tilde{\rho} \tag{28}$$

F. Boundary Conditions

The fundamental disparities between acoustic and vortical fields warrant the use of two dissimilar sets of boundary conditions. In the case of the acoustic wave, a closed boundary must be maintained, as usual, along all solid surfaces, including the injection site (i.e., at $r=1$, $z=0$ and $z=L/R$). In the case of the rotational wave, the no-slip condition at the headwall must be secured first and foremost, being the counterpart of the sidewall boundary in the inverted analog of an axially traveling wave within an elongated porous cylinder.[6] In both geometric configurations, the no slip condition is secured at the injecting surfaces which can be either the headwall or the sidewall of the simulated LRE or SRM, respectively. Along the non-injecting surface (i.e. sidewall here), slip may be permitted in the vortical wave formulation. At the downstream end of the chamber, $z=L/R$, the vortical wave remains bounded and, being sufficiently removed from the headwall, it may be assumed that its rotational effects persist no longer. Naturally, with the attenuation of the unsteady vorticity component, the vorticoacoustic wave reduces to its potential form. A summary of the physical constraints entailed in the resulting model is furnished in Table 1.

III. Solution

This section describes the boundary layer approach that we follow to reduce the time-dependent vortical system into a more manageable set. The ensuing formulations will be derived from first principles and for arbitrary mean flow profiles. In this vein, the acoustic wave motion will be considered first being primarily responsible for generating the unsteady vorticity field.

A. Acoustic Formulation

Although Eqs. (20)–(24) consist of an assortment of five equations, they can be systematically reduced to a single PDE that represents a modified form of the wave equation. By subtracting the derivative of the acoustic mass conservation from the divergence of the momentum equation, an extended form of the wave equation[1] is revealed, specifically:

$$\frac{\partial^2 \hat{p}}{\partial t^2} = \nabla^2 \hat{p} + M_b \left[\gamma \nabla^2 \left(\boldsymbol{U} \cdot \hat{\boldsymbol{u}} \right) - \gamma \nabla \cdot \left(\hat{\boldsymbol{u}} \times \bar{\boldsymbol{\Omega}} \right) - \frac{\partial}{\partial t} \left(\boldsymbol{U} \nabla \cdot \hat{p} \right) \right] \tag{29}$$

Several detailed solutions of Eq. (29) are widely available in the literature. In what follows, we employ a solution that suitably describes the acoustic motion in a simulated LRE, where transverse waves dominate over their longitudinal counterparts. In this case, the complete leading-order acoustic field may be reproduced from

$$\hat{p} = e^{-ik_{mn}t} J_m \left(k_{mn} r \right) \cos\left(m\theta \right) \tag{30}$$

$$\hat{u}_r = \frac{i}{k_{mn}\gamma} e^{-ik_{mn}t} J'_m \left(k_{mn} r \right) \cos\left(m\theta \right) \tag{31}$$

$$\hat{u}_\theta = \frac{i}{k_{mn}\gamma} \frac{m}{r} e^{-ik_{mn}t} J_m \left(k_{mn} r \right) \sin\left(m\theta \right) \tag{32}$$

$$\hat{u}_z = 0 \tag{33}$$

where m and n are positive integers that refer to the tangential and radial mode numbers, respectively. In the same vein, k_{mn} and m designate the radial and tangential wave numbers, and the numerical values of k_{mn} may be extracted from the roots of $J'(k_{mn}) = 0$. These return the transverse wave numbers that may be labelled as:

$$\begin{cases} k_{01} \approx 3.831\,705\,97 & k_{10} \approx 1.841\,183\,78 & k_{11} \approx 5.331\,442\,77 \\ k_{02} \approx 7.015\,586\,67 & k_{20} \approx 3.054\,236\,93 & k_{22} \approx 9.969\,467\,82 \\ k_{12} \approx 8.536\,316\,37 & k_{21} \approx 6.706\,133\,19 & \text{etc.} \end{cases} \tag{34}$$

In the interest of clarity, the four parts of Fig. 2 are intended to illustrate the instantaneous pressure distribution along with the acoustic velocity vectors in our right-cylindrical chamber using four sequential mode numbers. These relate to four zeroes of J'_m listed in Eq. (34). Everywhere, the pressure contours and velocity vectors represent snapshots taken in a polar plane at $t = 0.01$ s, $\forall z$, where red and blue colors denote positive and negative acoustic pressures, respectively. It may be interesting to note the evolution of the nodal lines going from a) to d), thus giving rise to double-D and alternating cross patterns that characterize the acoustic modes shapes. In a) and b), the first and second radial modes are featured along with the first tangential mode where alternating double-D contours appear either a) once or b) twice, with the second set brushing along the outer periphery. The corresponding velocity nodal lines are shifted at a 90 degree angle. In c) and d), the second tangential configuration is depicted at the first and second radial modes. The last contour clearly captures the symmetrically alternating wave structure in both tangential and radial directions. Consistently with the first cases considered, the velocity nodal lines appear to be at a 45 degree angle with respect to the pressure, thus leading to straight crosses (instead of oblique crosses) at $m = 2$. In comparison to the acoustic pressure distribution displayed in Fig. 2, the nodal lines of the vorticoacoustic waves are shifted by a phase angle of $\pi / (2m)$.

B. Vortical Formulation

Before proceeding with the formulation of the vortical wave structure, it may be useful to clarify the origin of the driving mechanisms for the waves in question, while paying particular attention to the reason for the decoupling of the incompressible continuity and momentum equations from the remaining members in Eqs. (25)–(28). To this end, we recall that the acoustic waves stem from pressure gradients within the chamber and these remain immune to the effects of the no-slip requirement at the boundaries. They also display no sensitivity to the mean flow when evaluated at the leading order in M_b. In contrast, the traveling vortical waves are generated by the acoustic motion due to the presence of solid boundaries. They appear as a necessary correction that depends on the geometry at hand, the mean flow, and the acoustic mode shapes. From this perspective, it may be argued that the vortical pressure distribution may be dismissed and this may be attributed to the pressure differential being mainly prescribed by the acoustic field.[5] The foregoing assumption will be useful while solving for the vortical disturbance. However, at this stage, we find it convenient to retain the small vortical pressure wave $\tilde{p}$ in the momentum equation as we put

$$\nabla \cdot \tilde{\boldsymbol{u}} = 0 \tag{35}$$

$$\frac{\partial \tilde{\boldsymbol{u}}}{\partial t} = -\frac{1}{\gamma} \nabla \tilde{p} - M_b \left[\nabla \left(\boldsymbol{U} \cdot \tilde{\boldsymbol{u}} \right) - \boldsymbol{U} \times \tilde{\boldsymbol{\omega}} - \tilde{\boldsymbol{u}} \times \bar{\boldsymbol{\Omega}} \right] - \delta^2 \nabla \times \tilde{\boldsymbol{\omega}} \tag{36}$$

In seeking an ansatz for $\tilde{\boldsymbol{u}}$, we note that in Eqs. (35)–(36), the rotational velocity disturbance stands as a function of time and three spatial variables. Moreover, it is necessary to choose $\tilde{\boldsymbol{u}}(t, r, \theta, z)$ in a manner to offset

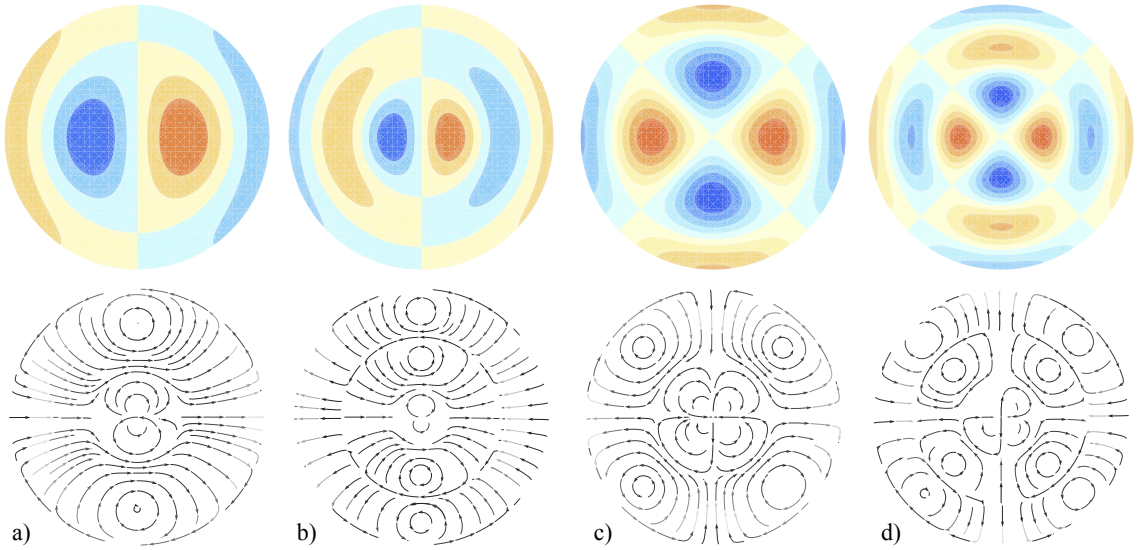

Figure 2. Pressure (upper) and velocity (lower) contours in a polar slice for transverse wave oscillations corresponding to: a) k_{11}, b) k_{12}, c) k_{21}, and d) k_{22}.

the acoustic motion at the headwall, $\forall t$. The time dependence of the vortical field will then match that of the acoustic motion in the injection plane. This can be achieved when the unsteady vortical wave exhibits the form

$$\tilde{\boldsymbol{u}} = e^{-ik_{mn}t} f(r,\theta,z) \quad \text{or} \quad \frac{\partial \tilde{\boldsymbol{u}}}{\partial t} = -ik_{mn} e^{-ik_{mn}t} f(r,\theta,z) = -ik_{mn}\tilde{\boldsymbol{u}} \tag{37}$$

This particular ansatz will be used to secure a closed-form vortical approximation.

C. Arbitrary Injection Profile

The transverse wave subject to a uniform mean flow is briefly explored by Fischbach, Flandro and Majdalani[1] as part of their investigation of the acoustic streaming mechanism in a simulated LRE. A more in-depth formulation that focuses on wave characterization is later furnished wherein detailed solutions for the uniform and bell-shaped injection profiles are carefully constructed.[2] The present approach will therefore apply a regular perturbation expansion to a well-established variant of the conservation equations. For the case of an arbitrary mean flow, Eqs. (35) and (36) may be expanded in scalar notation to produce

$$\frac{\tilde{u}_r}{r} + \frac{\partial \tilde{u}_r}{\partial r} + \frac{1}{r}\frac{\partial \tilde{u}_\theta}{\partial \theta} + \frac{\partial \tilde{u}_z}{\partial z} = 0 \tag{38}$$

$$-ik_{mn}\tilde{u}_r + M_b F \frac{\partial \tilde{u}_r}{\partial z} = -\frac{1}{\gamma}\frac{\partial \tilde{p}}{\partial r} + \delta^2\left(\frac{\partial^2 \tilde{u}_r}{\partial z^2} + \frac{1}{r^2}\frac{\partial^2 \tilde{u}_r}{\partial \theta^2} - \frac{1}{r^2}\frac{\partial \tilde{u}_\theta}{\partial \theta} - \frac{1}{r}\frac{\partial^2 \tilde{u}_\theta}{\partial r \partial \theta} - \frac{\partial^2 \tilde{u}_z}{\partial r \partial z}\right) \tag{39}$$

$$-ik_{mn}\tilde{u}_\theta + M_b F \frac{\partial \tilde{u}_\theta}{\partial z} = -\frac{1}{\gamma r}\frac{\partial \tilde{p}}{\partial \theta} + \delta^2\left(\frac{1}{r^2}\frac{\partial \tilde{u}_r}{\partial \theta} - \frac{1}{r}\frac{\partial^2 \tilde{u}_r}{\partial r \partial \theta} - \frac{\tilde{u}_\theta}{r^2} + \frac{\partial^2 \tilde{u}_\theta}{\partial z^2} + \frac{1}{r}\frac{\partial \tilde{u}_\theta}{\partial r} + \frac{\partial^2 \tilde{u}_\theta}{\partial r^2} - \frac{1}{r}\frac{\partial^2 \tilde{u}_z}{\partial \theta \partial z}\right) \tag{40}$$

$$-ik_{mn}\tilde{u}_z + M_b F \frac{\partial \tilde{u}_z}{\partial z} - M_b F' \tilde{u}_r = -\frac{1}{\gamma}\frac{\partial \tilde{p}}{\partial z} + \delta^2\left(-\frac{1}{r}\frac{\partial \tilde{u}_r}{\partial z} - \frac{\partial^2 \tilde{u}_r}{\partial r \partial z} - \frac{1}{r}\frac{\partial^2 \tilde{u}_\theta}{\partial \theta \partial z} + \frac{1}{r^2}\frac{\partial^2 \tilde{u}_z}{\partial \theta^2} + \frac{1}{r}\frac{\partial \tilde{u}_z}{\partial r} + \frac{\partial^2 \tilde{u}_z}{\partial r^2}\right) \tag{41}$$

Recognizing that the vortical wave is most noticeable near solid surfaces, Eqs. (38)–(41) may be transformed using boundary layer theory, with the no-slip boundary condition being enforced at the headwall. Because the vortical wave can grow or decay in the axial direction, it is helpful to rescale the axial variable using a stretched inner coordinate of the form

$$\zeta = \frac{z}{\delta} \tag{42}$$

This spatial distortion is necessary because the near-wall boundary layer correction cannot be captured with the original variable z. Rescaling the axial coordinate serves a similar purpose to zooming onto the near wall region; only then would the inner behavior of the solution be revealed. The outer inviscid solution remains adequate except

in the boundary layer region where viscous forces dominate. Moreover, being the inverted square root of the acoustic Reynolds number, the viscous parameter $\delta << 1$ can be suitably employed as a perturbation parameter. On this note, our subsequent step consists of expanding the vortical variables that appear in Eqs. (38)–(41) with respect to the viscous parameter. This is accomplished by setting

$$\tilde{q} = \tilde{q}^{(0)} + \delta\tilde{q}^{(1)} + \delta^2\tilde{q}^{(2)} + \delta^3\tilde{q}^{(3)} + \mathcal{O}(\delta^4) \tag{43}$$

The process of collecting terms of the same order in δ and rearranging leads to two vortical sets that must be solved in succession. In so doing, caution is to be exercised while handling terms of order M_b/δ. Because the Mach number and viscous parameters can appear at about the same order, their ratio can be of order unity and, hence, non-negligible.

1. Leading-Order Solution

At $\mathcal{O}(1)$, Eqs. (38)–(41) render

$$\frac{\partial\tilde{u}_\zeta^{(0)}}{\partial\zeta} = 0 \tag{44}$$

$$-ik_{mn}\tilde{u}_r^{(0)} + \frac{M_b}{\delta}F\frac{\partial\tilde{u}_r^{(0)}}{\partial\zeta} - \frac{\partial^2\tilde{u}_r^{(0)}}{\partial\zeta^2} = -\frac{1}{\gamma}\frac{\partial\tilde{p}^{(0)}}{\partial r} \tag{45}$$

$$-ik_{mn}\tilde{u}_\theta^{(0)} + \frac{M_b}{\delta}F\frac{\partial\tilde{u}_\theta^{(0)}}{\partial\zeta} - \frac{\partial^2\tilde{u}_\theta^{(0)}}{\partial\zeta^2} = -\frac{1}{\gamma r}\frac{\partial\tilde{p}^{(0)}}{\partial\theta} \tag{46}$$

$$\frac{1}{\gamma}\frac{\partial\tilde{p}^{(0)}}{\partial\zeta} = 0 \tag{47}$$

Clearly, Eqs. (44)–(47) appear to be nearly decoupled, with the exception of the vortical pressure term appearing on the right-hand side of both the radial and tangential equations. Solving Eq. (47) yields an axially invariant $\tilde{p}^{(0)} = \tilde{p}^{(0)}(t,r,\theta)$. At this order, the no-slip condition at the headwall may be viewed as the main driver behind the bulk axial propagation of the vortical wave. The vortical pressure remains immaterial to the wave generated and can be set equal to zero. We therefore take

$$\tilde{p}^{(0)} = 0 \tag{48}$$

Similarly, solving Eq. (44) leads to an axially invariant $\tilde{u}_\zeta^{(0)}$ that must be suppressed in order to satisfy the no-slip condition at the headwall. This is performed by putting

$$\tilde{u}_\zeta^{(0)} = G_{\zeta 0}(r,\theta) = 0 \tag{49}$$

Now that $\tilde{p}^{(0)}$ has been settled, Eqs. (45) and (46) can be collapsed into a single equation. The general solution of the resulting ODE proves to be identical for both velocities. The differences emerge when applying the boundary conditions corresponding to each vortical component. For example, either radial or tangential equations reduce to

$$-ik_{mn}\tilde{u}_{r,\theta}^{(0)} + \frac{M_b}{\delta}F\frac{\partial\tilde{u}_{r,\theta}^{(0)}}{\partial\zeta} - \frac{\partial^2\tilde{u}_{r,\theta}^{(0)}}{\partial\zeta^2} = 0 \tag{50}$$

and so

$$\tilde{u}_{r,\theta}^{(0)} = A_{r,\theta}^{(0)}(t,r,\theta)e^{X_1\zeta} + B_{r,\theta}^{(0)}(t,r,\theta)e^{X_2\zeta} \tag{51}$$

where the axial constants X_1 and X_2 depend on the injection profile, F, and are thus functions of the radial variable, r:

$$X_1(r) = \frac{M_b}{2\delta}\left(1 - \sqrt{1 - \frac{4ik_{mn}\delta^2}{M_b^2F^2}}\right) \tag{52}$$

$$X_2(r) = \frac{M_b}{2\delta}\left(1 + \sqrt{1 - \frac{4ik_{mn}\delta^2}{M_b^2F^2}}\right) \tag{53}$$

At this juncture, two physical constraints may be brought to bear: the physicality of the solution in the farfield and the no-slip requirement at the headwall. First, in order to determine which of the axial constants provides a physical solution, Eqs. (52) and (53) may be rewritten in such a way to explicitly isolate their real and imaginary parts. We retrieve

$$X_1(r)=\frac{M_b}{2\delta}\left(1-\sqrt{\frac{1}{2}+\frac{1}{2}\sqrt{1+\frac{16k_{mn}^2\delta^4}{M_b^4F^4}}}+i\sqrt{\frac{1}{2}\sqrt{1+\frac{16k_{mn}^2\delta^4}{M_b^4F^4}}-\frac{1}{2}}\right) \tag{54}$$

$$X_2(r)=\frac{M_b}{2\delta}\left(1+\sqrt{\frac{1}{2}+\frac{1}{2}\sqrt{1+\frac{16k_{mn}^2\delta^4}{M_b^4F^4}}}-i\sqrt{\frac{1}{2}\sqrt{1+\frac{16k_{mn}^2\delta^4}{M_b^4F^4}}-\frac{1}{2}}\right) \tag{55}$$

Recalling that $F\geq 0$ in the domain of interest, its presence is immaterial to the sign of X_2; the latter, having a positive real component, can cause the vortical velocities to grow unboundedly for large ζ. Therefore, $B_{r,\theta}^{(0)}(r,\theta,t)$ must be suppressed to prevent the unphysical growth of the velocities as $\zeta\to\infty$ in the farfield. Equation (51) becomes

$$\tilde{u}_{r,\theta}^{(0)}=A_{r,\theta}^{(0)}(t,r,\theta)e^{X_1\zeta} \tag{56}$$

Finally, the velocity adherence condition at the headwall ($\zeta=0$) can be applied to each velocity component separately. This enables us to fully determine the radial and tangential components,

$$\tilde{u}_r^{(0)}=-\frac{i}{k_{mn}\gamma}e^{-ik_{mn}t}e^{X_1\zeta}\cos(m\theta)J_m'(k_{mn}r) \tag{57}$$

$$\tilde{u}_\theta^{(0)}=-\frac{i}{k_{mn}\gamma}\frac{m}{r}e^{-ik_{mn}t}e^{X_1\zeta}\sin(m\theta)J_m(k_{mn}r) \tag{58}$$

2. First-Order Solution

At $\mathcal{O}(\delta)$, Eqs. (38)–(41) lead to

$$\frac{\partial\tilde{u}_\zeta^{(1)}}{\partial\zeta}=-\frac{1}{r}\tilde{u}_r^{(0)}-\frac{\partial\tilde{u}_r^{(0)}}{\partial r}-\frac{1}{r}\frac{\partial\tilde{u}_\theta^{(0)}}{\partial\theta} \tag{59}$$

$$ik_{mn}\tilde{u}_r^{(1)}-\frac{M_b}{\delta}F\frac{\partial\tilde{u}_r^{(1)}}{\partial\zeta}+\frac{\partial^2\tilde{u}_r^{(1)}}{\partial\zeta^2}=\frac{1}{\gamma}\frac{\partial\tilde{p}^{(1)}}{\partial r}+\frac{\partial^2\tilde{u}_\zeta^{(0)}}{\partial r\partial\zeta} \tag{60}$$

$$ik_{mn}\tilde{u}_\theta^{(1)}-\frac{M_b}{\delta}F\frac{\partial\tilde{u}_\theta^{(1)}}{\partial\zeta}+\frac{\partial^2\tilde{u}_\theta^{(1)}}{\partial\zeta^2}=-\frac{1}{\gamma r}\frac{\partial\tilde{p}^{(1)}}{\partial\theta}+\frac{1}{r}\frac{\partial^2\tilde{u}_\zeta^{(0)}}{\partial\theta\partial\zeta} \tag{61}$$

$$\frac{1}{\gamma}\frac{\partial\tilde{p}^{(1)}}{\partial\zeta}=ik_{mn}\tilde{u}_\zeta{}^{(0)}-\frac{M_b}{\delta}F\frac{\partial\tilde{u}_\zeta^{(0)}}{\partial\zeta} \tag{62}$$

Given their origination from a perturbation expansion, Eqs. (59)–(62) mirror the leading-order set. Their left-hand side matches their predecessor's with the exception of being one order higher; their right-hand side accounts for the contributions stemming from the leading-order correction. With no further ado, the known vortical velocities and pressure may be substituted into Eqs. (59)–(62) to the extent of transforming the original system into:

$$\frac{\partial\tilde{u}_\zeta^{(1)}}{\partial\zeta}=\frac{i}{\gamma k_{mn}}e^{-ik_{mn}t}\left[k_{mn}^2J_m(k_{mn}r)e^{X_{1C}\zeta}-\zeta e^{X_{1C}\zeta}X_1'J_m'(k_{mn}r)\right]\cos(m\theta) \tag{63}$$

$$ik_{mn}\tilde{u}_r^{(1)}-\frac{M_b}{\delta}F\frac{\partial\tilde{u}_r^{(1)}}{\partial\zeta}+\frac{\partial^2\tilde{u}_r^{(1)}}{\partial\zeta^2}=\frac{1}{\gamma}\frac{\partial\tilde{p}^{(1)}}{\partial r} \tag{64}$$

$$ik_{mn}\tilde{u}_\theta^{(1)}-\frac{M_b}{\delta}F\frac{\partial\tilde{u}_\theta^{(1)}}{\partial\zeta}+\frac{\partial^2\tilde{u}_\theta^{(1)}}{\partial\zeta^2}=-\frac{1}{\gamma r}\frac{\partial\tilde{p}^{(1)}}{\partial\theta} \tag{65}$$

$$\frac{\partial\tilde{p}^{(1)}}{\partial\zeta}=0 \tag{66}$$

As before, the first-order vortical pressure can be resolved first, thus simplifying the solution of the remaining velocities. Obviously, the integration of Eq. (66) produces an axially invariant first-order pseudo-pressure. With no loss of generality, one may justifiably take

$$\tilde{p}^{(1)}=0 \tag{67}$$

Eliminating $\tilde{p}^{(1)}$ in Eqs. (64) and (65) leads to a homogeneous PDE for the radial and tangential components, namely,

$$ik_{mn}\tilde{u}_{r,\theta}^{(1)} - \frac{M_b}{\delta}\frac{\partial \tilde{u}_{r,\theta}^{(1)}}{\partial \zeta} + \frac{\partial^2 \tilde{u}_{r,\theta}^{(1)}}{\partial \zeta^2} = 0 \tag{68}$$

A solution to Eq. (68) that imitates that of Eq. (50) may be readily realized. To ensure boundedness in the domain of interest, especially as $\zeta \to \infty$, we deduce

$$\tilde{u}_{r,\theta}^{(1)} = A_{r,\theta}^{(1)}(t,r,\theta)e^{X_1\zeta} \tag{69}$$

Here too, the no-slip condition must be secured. However, since the cancellation of the acoustic velocity has been accomplished at the leading order, the first-order contribution at the headwall vanishes. This leaves us with

$$\tilde{u}_{r,\theta}^{(1)}(t,r,\theta,0) = A_{r,\theta}^{(1)} = 0 \tag{70}$$

and so

$$\tilde{u}_r^{(1)} = \tilde{u}_\theta^{(1)} = 0 \tag{71}$$

At this juncture, the axial component may be obtained through integration of Eq. (63) with respect to the stretched axial coordinate. This operation yields

$$\tilde{u}_\zeta^{(1)} = \frac{i}{\gamma k_{mn} X_1} e^{-ik_{mn}t}\left[k_{mn}^2 J_m(k_{mn}r)e^{X_1\zeta} - \left(\zeta e^{X_1\zeta}X_1 - e^{X_1\zeta}\right)\frac{X_1'}{X_1}J_m'(k_{mn}r)\right]\cos(m\theta) + A_\zeta^{(1)}(t,r,\theta) \tag{72}$$

In the above, the headwall boundary condition enables us to identify the integration constant $A_\zeta^{(1)}$. Its backward substitution into Eq. (72) leads to the first-order axial velocity,

$$\tilde{u}_\zeta^{(1)} = \frac{i}{\gamma k_{mn} X_1} e^{-ik_{mn}t}\left[k_{mn}^2 J_m(k_{mn}r)\left(e^{X_1\zeta}-1\right) - \left(\zeta e^{X_1\zeta}X_1 + 1 - e^{X_1\zeta}\right)\frac{X_1'}{X_1}J_m'(k_{mn}r)\right]\cos(m\theta) \tag{73}$$

Here X_1' denotes the derivative of X_1 with respect to r. This parameter is heavily dependent on the injection profile $F(r)$, viz.

$$X_1' = \frac{\partial X_1}{\partial r} = -\frac{\delta}{M_b}\frac{2ik_{mn}rF'}{F^3\sqrt{1-4ik_{mn}\delta^2 M_b^{-2}F^{-2}}} \tag{74}$$

IV. Results and Discussion

The analytical approximations obtained heretofore may be compiled into one set of expressions for the vorticoacoustic velocity and pressure distributions. The significance of these solutions and the behavior of their corresponding waves will now be discussed. In the process, the wave behavior associated with each of the mean flow profiles will be compared and contrasted.

In the interest of clarity, a summary of the vorticoacoustic wave components is provided by superimposing both potential and rotational contributions. The resulting unsteady disturbances may be asymptotically presented as:

$$p' = e^{-ik_{mn}t}J_m(k_{mn}r)\cos(m\theta) + \mathcal{O}(M_b,\delta^2) \tag{75}$$

$$u_r' = \frac{i}{k_{mn}\gamma}e^{-ik_{mn}t}J_m'(k_{mn}r)\cos(m\theta)\left(1-e^{X_1\zeta}\right) + \mathcal{O}(M_b,\delta^2) \tag{76}$$

$$u_\theta' = \frac{i}{k_{mn}\gamma}\frac{m}{r}e^{-ik_{mn}t}J_m(k_{mn}r)\sin(m\theta)\left(1-e^{X_1\zeta}\right) + \mathcal{O}(M_b,\delta^2) \tag{77}$$

$$u_z' = \frac{i}{k_{mn}\gamma}\frac{\delta}{X_1}e^{-ik_{mn}t}\cos(m\theta)\left[k_{mn}^2 J_m(k_{mn}r)\left(e^{X_1\zeta}-1\right) - \frac{X_1'}{X_1}J_m'(k_{mn}r)\left(\zeta e^{X_1\zeta}X_1 + 1 - e^{X_1\zeta}\right)\right] + \mathcal{O}(\delta^3) \tag{78}$$

A. Validation of Generalized Solution

Before proceeding with the analysis of the physical implications of Eqs. (75)–(78), it may be helpful to entertain a limiting process verification. Having served as the subjects of past investigations,[1,2] the uniform and bell-shaped injection profiles are chosen as test cases. The uniform injection case was first investigated by Fischbach, Flandro and Majdalani[1] and then reaffirmed by Haddad and Majdalani.[2] In both studies, the vorticoacoustic waves can be written as

$$p' = e^{-ik_{mn}t}J_m(k_{mn}r)\cos(m\theta) + \mathcal{O}(M_b,\delta^2) \tag{79}$$

$$u_r' = \frac{i}{k_{mn}\gamma} e^{-ik_{mn}t} J_m'\left(k_{mn}r\right)\cos\left(m\theta\right)\left(1-e^{X_{1U}\zeta}\right)+\mathcal{O}(M_b,\delta^2) \tag{80}$$

$$u_\theta' = \frac{i}{k_{mn}\gamma}\frac{m}{r} e^{-ik_{mn}t} J_m\left(k_{mn}r\right)\sin\left(m\theta\right)\left(1-e^{X_{1U}\zeta}\right)+\mathcal{O}(M_b,\delta^2) \tag{81}$$

$$u_z' = \frac{ik_{mn}}{\gamma}\frac{\delta}{X_{1U}} e^{-ik_{mn}t}\cos\left(m\theta\right) J_m\left(k_{mn}r\right)\left(e^{X_{1U}\zeta}-1\right)+\mathcal{O}(\delta^3) \tag{82}$$

where $X_{1U} = \frac{1}{2}M_b\delta^{-1}(1-\sqrt{1-4ik_{mn}\delta^2 M_b^{-2}})$.

When comparing Eqs. (79)–(82) to Eqs. (75)–(78), three conclusions may be drawn. Firstly, the total vorticoacoustic pressure will coincide with the acoustic pressure, which is common to all cases considered. It remains independent of the injection profile unless higher orders in M_b^2 are sought. Secondly, the vorticoacoustic radial and tangential velocities in Eqs. (80) and (81) will match those of the generalized solution whenever their axial parameters concur. In this context, it can be readily verified that X_{1U} is recoverable from X_1 following a straightforward substitution of the injection profile F by its unit value. Thirdly, the most noticeable difference arises in the expression of the axial vorticoacoustic velocity. Despite visible dissimilarities, it may be shown that Eq. (82) will duplicate Eq. (78) when X_1 is replaced by X_{1U}. Subsequently, the constant value of X_{1U} will lead to a vanishing X_{1U}', thus restoring the form obtained in previous work.

Our next step consists of comparing the generalized solution to that of the bell-shaped injection profile. As described by Haddad and Majdalani,[2] the vorticoacoustic wave generated by the bell-shaped injection profile may be expressed as

$$p' = e^{-ik_{mn}t} J_m\left(k_{mn}r\right)\cos\left(m\theta\right)+\mathcal{O}(M_b,\delta^2) \tag{83}$$

$$u_r' = \frac{i}{k_{mn}\gamma} e^{-ik_{mn}t} J_m'\left(k_{mn}r\right)\cos\left(m\theta\right)\left(1-e^{X_{1C}\zeta}\right)+\mathcal{O}(M_b,\delta^2) \tag{84}$$

$$u_\theta' = \frac{i}{k_{mn}\gamma}\frac{m}{r} e^{-ik_{mn}t} J_m\left(k_{mn}r\right)\sin\left(m\theta\right)\left(1-e^{X_{1C}\zeta}\right)+\mathcal{O}(M_b,\delta^2) \tag{85}$$

$$u_z' = \frac{i}{k_{mn}\gamma}\frac{\delta}{X_{1C}} e^{-ik_{mn}t}\cos\left(m\theta\right)\left[\begin{array}{l} k_{mn}^2 J_m\left(k_{mn}r\right)\left(e^{X_{1C}\zeta}-1\right) \\ -\dfrac{X_{1C}'}{X_{1C}} J_m'\left(k_{mn}r\right)\left(\zeta e^{X_{1C}\zeta}X_{1C}+1-e^{X_{1C}\zeta}\right)\end{array}\right]+\mathcal{O}(\delta^3) \tag{86}$$

where $X_{1C} = \frac{1}{2}M_b\delta^{-1}[1-\sqrt{1-4ik_{mn}\delta^2 M_b^{-2}\sec^2(\frac{1}{2}\pi r^2)}]$.

Verifying that Eqs. (83)–(86) may be restored from their generic counterparts can be readily accomplished, especially that their expressions become identical when X_{1C} replaces X_1. For the case in question, the axial parameters coincide when the injection profile F is substituted by the bell-shaped expression, $\cos(\frac{1}{2}\pi r^2)$.

In addition to the uniform and bell-shaped profiles, two new cases are examined here. These correspond to the classical laminar and turbulent profiles in a cylindrical enclosure. The combined cases hence provide four different chamber scenarios whose properties may be compared. For the sake of illustration, the plots in Figs. 3–5 are used to display the behavior of the radial, tangential and axial disturbances along the chamber axis at decreasing values of the inlet Mach number. To remain consistent with former work on the subject, our comparisons are drawn for $t = 0$, $\delta = 0.000647$, and a thrust chamber whose aspect ratio is equal to unity ($z_{\text{exit}} = L/R = 1$).[1,2] To this end, Figs. 3–5 are used to capture the oscillatory motion at $r = 1/\sqrt{2}$ and $\theta = \frac{1}{4}\pi$ for the first tangential and radial modes corresponding to $k_{11} \approx 5.331$. In addition, each of these plots displays the unsteady velocities at two inlet Mach numbers of $M_b = 0.3$ and 0.003.

B. Wave Characterization

As alluded to previously, the expressions for unsteady radial and tangential velocities in Eqs. (76) and (77) are nearly identical for all test cases. This behavior may be observed in the foregoing illustrations. The effect of specific mean flow motion is manifested through the axial parameter X_1; except for this mean flow dissimilarity, the approximations obtained in the radial and tangential directions would have concurred identically. Their spatial distributions are therefore expected to behave similarly, with minor shifts that are caused by differences in their mean flow speeds, an observation that is confirmed through Figs. 3–5. For instance, at $r = 0.7$, the mean flow velocity returns a value of unity for the uniform flow and 0.7181, 0.51, and 0.8420 for the bell-shaped, laminar,

and turbulent profiles, respectively. It may hence be seen that slower downstream propagation of the unsteady traveling waves may be attributed to slower injection velocities. According to Table 2, the fastest injection speed at $r = 0.7$ belongs to the uniform injection profile and is followed, in decreasing order, by the turbulent, bell-shaped, and laminar profiles. Correspondingly, the individual plots in Fig. 3 show that the radial waves are swept downstream at speeds that are commensurate with the headwall injection pattern of the model in question.

The behavior of the vortical component in the axial direction deserves particular attention. Recalling that the acoustic component of the axial wave is discounted here (assuming a short chamber), the unsteady axial wave, u_z', becomes confounded with the vortical part, $\tilde{u}_z$. The latter is needed to compensate for the more dominant tangential and radial components and, thereby, ensure that continuity is fully satisfied. Figure 5 illustrates the behavior of u_z' for two injection Mach numbers. In these snapshots, the average unsteady velocity appears to be negative in the uniform injection case and positive for the bell-shaped, laminar, and turbulent flow models. Furthermore, the absolute value of the velocity remains higher for the laminar and bell-shaped cases. This behavior may be attributed to the speed of the mean flow at $r = 0.7$, where the bell-shaped and laminar patterns, in comparison to the uniform and turbulent motions, possess less kinetic energy for inducing the traveling wave

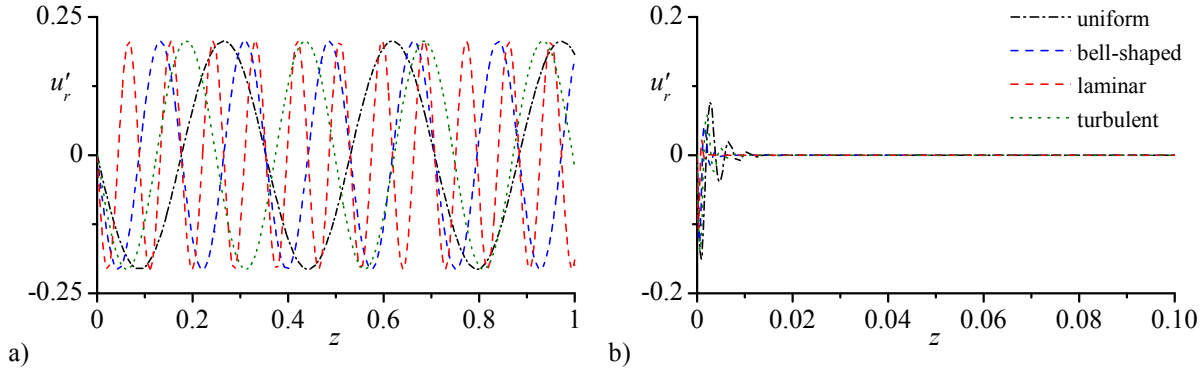

Figure 3. Unsteady radial velocity at inlet Mach numbers corresponding to a) 0.3 and b) 0.003.

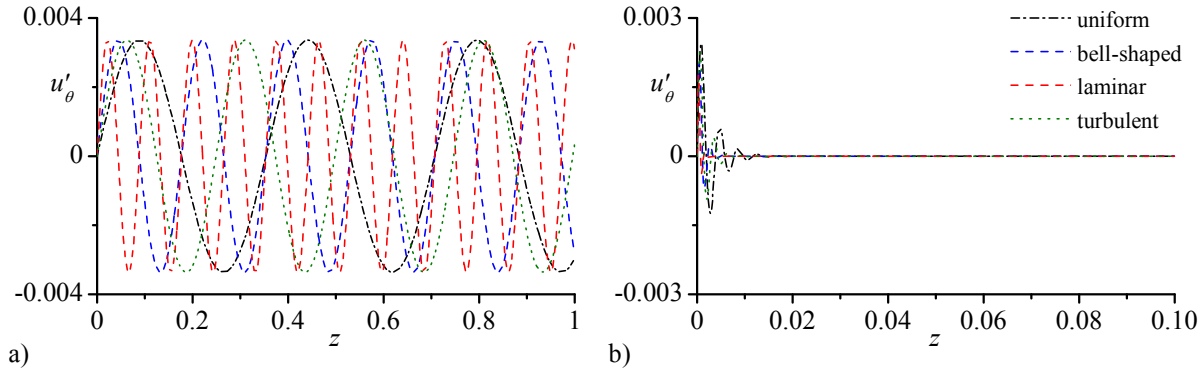

Figure 4. Unsteady tangential velocity at inlet Mach numbers corresponding to a) 0.3 and b) 0.003.

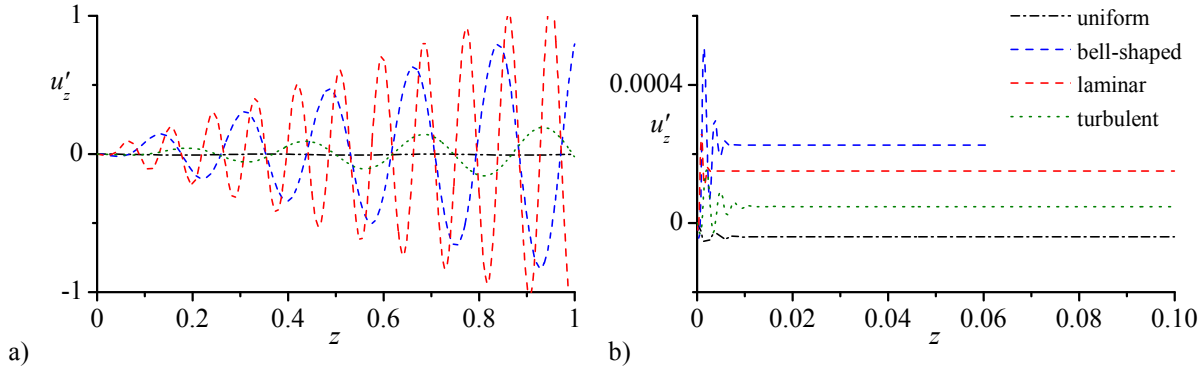

Figure 5. Unsteady axial velocities at inlet Mach numbers corresponding to a) 0.3 and b) 0.003.

Table 2. Axial speeds at $r = 0.7$ for the four representative headwall injection profiles

Injection profile	Expression	Speed at $r = 0.7$	Speed ranking
Uniform	1	1	1
Bell-shaped	$\cos(\frac{1}{2}\pi r^2)$	0.7181	3
Laminar	$1-r^2$	0.51	4
Turbulent	$(1-r)^{1/7}$	0.8420	2

motion. At the outset, they are accompanied by a faster spatial attenuation of their wave amplitudes.

To further confirm this feature, an inspection of the axial parameter X_1 in Eq. (52) shows that, at the centerline, the profile function F for the bell-shaped, laminar, and turbulent cases will consistently yield a value of unity that matches the result for the uniform flow case. Moreover, as we move away toward the sidewall, $F \to 0$. In close proximity of the sidewall, $X_1 \to -\infty$, having a negative real part. It may therefore be seen that at the sidewall, Eqs. (76)–(78) collapse into

$$u_r' = 0 + \mathcal{O}(M_b, \delta^2) \tag{87}$$

$$u_\theta' = \frac{im}{k_{mn}\gamma} e^{-ik_{mn}t} J_m\left(k_{mn}\right) \sin\left(m\theta\right) + \mathcal{O}(M_b, \delta^2) \tag{88}$$

$$u_z' = 0 + \mathcal{O}(\delta^3) \tag{89}$$

Equations (87) and (89) confirm that through the use of a mean flow profile function that vanishes at $r = 1$, the ensuing transverse wave motion can intrinsically satisfy the no-slip requirement, not only at the headwall but at the sidewall as well. This is true of the dominant component of the wave, u_r', and of u_z' as well. As for the contribution of u_θ', its value at the sidewall remains identical to that of the acoustic component and this may be attributed to the vortical contribution in the tangential direction becoming vanishingly small at $r = 1$.

C. Penetration Number and Rotational Layer Thickness

Figures 3–5 illustrate the dependence of the wave's boundary layer thickness on the injection Mach number. It is apparent that viscous forces dominate over inertial forces as the injection Mach number is reduced. Conversely, when the injection Mach number is successively augmented, it may be seen that the rotational boundary layer becomes more appreciably blown off the headwall.[34] Along similar lines, the slower decay of the wave due to a higher Mach number results in a larger propagation wavelength as measured by its peak-to-peak value.

Physically, the behavior of the propagation wavelength may be attributed to the wave's Strouhal number, or dimensionless frequency, $S = k_{mn} / M_b$. A decrement in the injection Mach number and its corresponding increment in the Strouhal number lead to a larger number of reversals per unit time. Furthermore, the increased frequency results in a higher interaction rate between fluid particles, and it is this increased friction between shear layers that leads to a more rapid attenuation of the wave amplitude.

Mathematically, the same behavior may be deduced by rewriting the axial decay term X_1 of Eq. (52) in terms of the Strouhal number and another dimensionless parameter. On this note, a two-term Maclaurin series approximation of X_1 is helpful to capture the amplitude (real) and oscillatory (imaginary) components of the wave. These are

$$X_1 \approx i\frac{k_{mn}\delta}{M_b F} - \frac{k_{mn}^2\delta^3}{M_b^3 F^2} = \delta\left(i\frac{S}{F} - \frac{1}{S_p F^2}\right) \tag{90}$$

where the effective penetration number S_p emerges in the form

$$S_p = \frac{M_b^3}{k_{mn}^2\delta^2} = \left(\frac{U_b^3}{a_0^3}\right)\left(\frac{a_0 R}{\nu_0}\right)\left(\frac{a_0^2}{\omega_{mn}^2 R^2}\right) = \frac{U_b^3}{\omega_{mn}^2 \nu_0 R} = \frac{1}{4\pi^2}\frac{U_b^3}{f_{mn}^2 \nu_0 R} \tag{91}$$

This parameter played a key role in the characterization of the boundary layer thickness of the longitudinal vorticoacoustic wave in a simulated SRM.[21] Note that an increase in S_p leads to a deeper penetration of the wave. From a theoretical standpoint, the penetration number gauges the relative intensity of two basic forces: unsteady inertia and viscous diffusion of the (comparable) radial and tangential velocities in the axial direction. For the radial and tangential velocities, S_p may be viewed as the ratio of

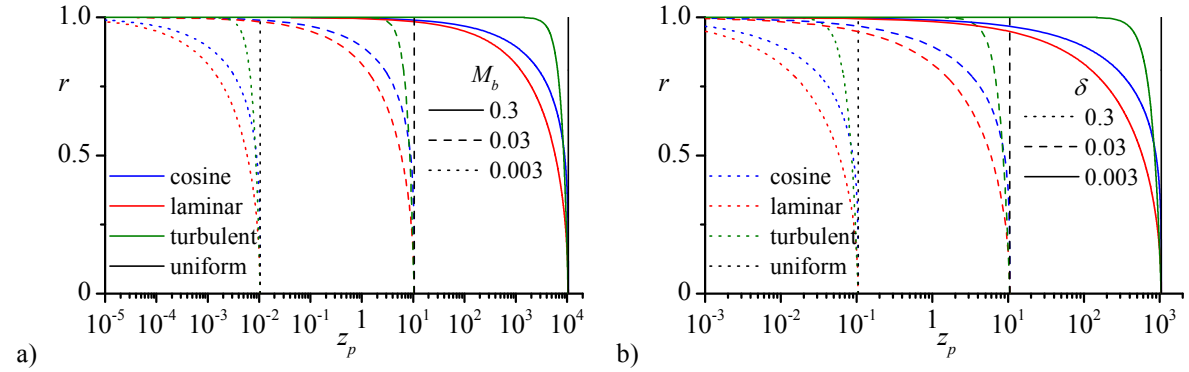

Figure 6. Sensitivity of the penetration depth to variations in blowing speed and viscosity shown at a) constant $\delta = 0.000647$ and b) $M_b = 0.03$ using the bell-shaped, laminar, turbulent, and uniform injection profiles.

$$\frac{\text{unsteady inertial force}}{\text{viscous force}} \approx \frac{\dfrac{\partial u^*_{r,\theta}}{\partial t^*}}{\nu \dfrac{\partial^2 u^*_{r,\theta}}{\partial z^{*2}}} \approx \frac{\dfrac{u^*_{r,\theta}}{t^*}}{\nu \dfrac{u^*_{r,\theta}}{z^{*2}}} = \frac{z^{*2}}{\nu t^*} \approx \frac{(U_b/\omega_{mn})^2}{\nu (R/U_b)} = \frac{U_b^3}{\omega_{mn}^2 \nu_0 R} = S_p \tag{92}$$

To showcase the significance of these dimensionless groupings, the wave expressions may be recast using the Strouhal and penetration numbers. At the outset, the (real) magnitudes of the waves in Eqs. (76)–(78) become simply dependent on

$$u'_r \sim J'_m(k_{mn} r)\left[1 - \exp\left(-\frac{z}{S_p F^2}\right)\right] \tag{93}$$

$$u'_\theta \sim J_m(k_{mn} r)\left[1 - \exp\left(-\frac{z}{S_p F^2}\right)\right] \tag{94}$$

and

$$u'_z \sim S_p F^2 \left\{ k_{mn}^2 J_m(k_{mn} r)\left[\exp\left(-\frac{z}{S_p F^2}\right) - 1\right] + 2\frac{F'}{F} J'_m(k_{mn} r)\left[\frac{z}{S_p F^2}\exp\left(-\frac{z}{S_p F^2}\right) - \exp\left(-\frac{z}{S_p F^2}\right) + 1\right]\right\} \tag{95}$$

A straightforward inspection of Eqs. (93) and (94) confirms that, at the sidewall, the radial component vanishes while the tangential component scales with $J_m(k_{mn})$. Naturally, these observations are well consistent with the asymptotic behavior of the waves at the boundaries. Along similar lines, two terms in Eq. (95) ensure the cancellation of the axial component at the sidewall. Examining the three terms between braces further reveals that the vanishing F^2 multiplier along with the limiting value of $J'_m(k_{mn} r)/F$ as $r \to 1$ ensure the satisfaction of the no-slip boundary condition at the sidewall.

To more effectively characterize the spread of unsteady vorticity in the chamber, the rotational boundary layer may be deduced from Eqs. (93) and (94). The penetration of rotational elements is defined as the distance from the injecting boundary to the point where the contribution of the vortical wave becomes negligible, a condition that is traditionally taken at 1% of the acoustic wave.[34] Because the axial component of the potential field vanishes in the farfield, the penetration depth may be extracted for the radial and tangential components by putting:

$$e^{-\frac{z}{S_p F^2}} = \alpha = 0.01 \tag{96}$$

where α corresponds to 1% and z_p denotes the axial thickness of the rotational boundary layer. Rearranging Eq. (96) renders a closed-form expression for z_p, namely,

$$z_p = S_p F^2 \ln(\alpha^{-1}) = \frac{M_b^3}{k_{mn}^2 \delta^2} F^2 \ln(\alpha^{-1}) \tag{97}$$

Figure 6 correlates the thickness of the vorticoacoustic boundary layer to the injection Mach number and viscous parameter. In conjunction with the expression obtained in Eq. (97), Fig. 6 shows that the boundary layer thickens for large injection Mach numbers, with the potential of exceeding the length of the chamber. When this situation

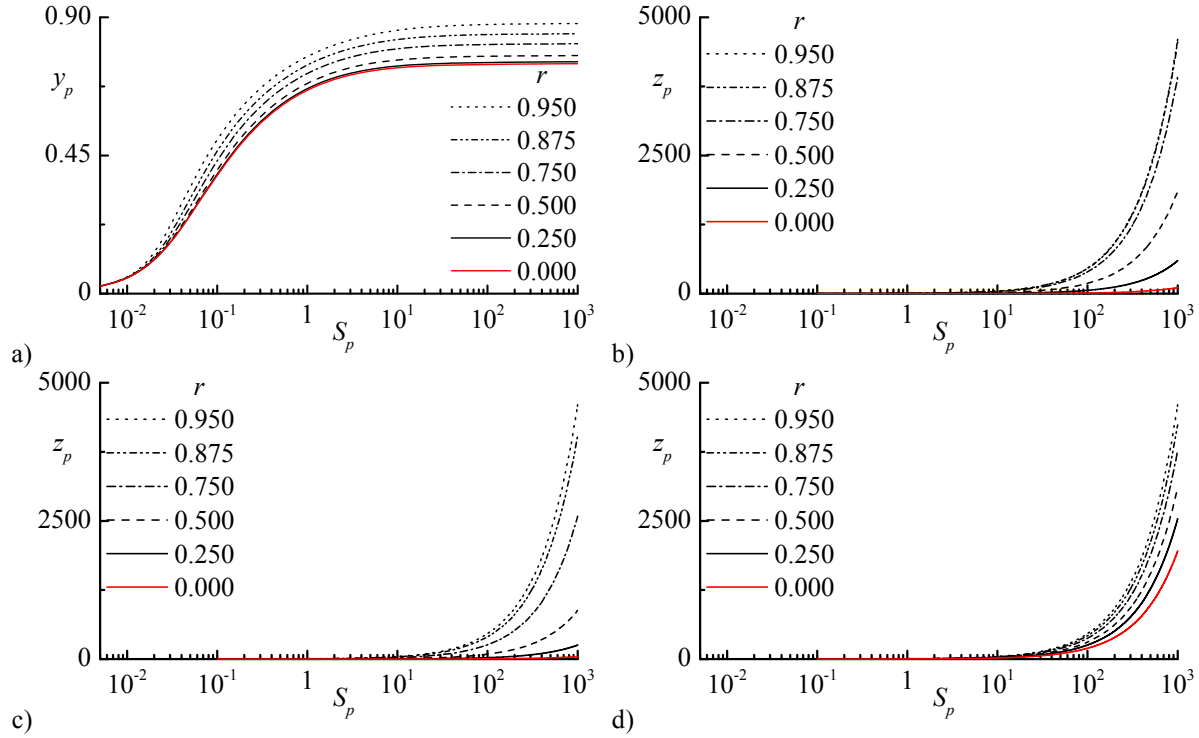

Figure 7. Penetration depths of vortical waves corresponding to a) longitudinal oscillations in long SRM configurations[34] versus transverse waves in short LRE chambers using b) bell-shaped, c) laminar, and d) turbulent injection profiles.

occurs, the linear oscillations will have no time to depreciate before exiting the chamber; the latter would be entirely filled with high amplitude transverse waves. On the other hand, in the case of small injection Mach numbers, the onset of transverse oscillations will remain almost exclusively limited to the vicinity of the injector zone. Rotational effects will fade elsewhere.

Based on $z_p \sim F^2$, the dependence on the injection pattern is apparent in the expression of the penetration depth. In the bell-shaped, laminar, and turbulent cases, the boundary layer thickness reaches its peak value at the centerline, where disturbances are swept into the chamber with the largest headwall velocity, acting here as a tailwind. However, the thickness of this region depreciates precipitously down to zero at the sidewall where the mean flow is nil. This behavior cannot be mimicked by the uniform profile for which the penetration depth remains constant throughout the chamber, a result that may not be entirely physical.

Figure 7a showcases the dependence of y_p on the penetration number and axial chamber position in the SRM case. Figures 7b, 7c and 7d illustrate a similar dependence of z_p in the LRE case, where the effects of the different injection mechanisms are encapsulated. In SRMs, particles injected radially at the sidewall must turn before merging in the longitudinal direction. This causes the penetration depth to increase in the direction along which unsteady vorticity is swept (downstream) by virtue of the mean flow. Conversely, in LRE thrust chambers, injection takes place at the headwall and remains unaffected by the downstream convection of unsteady vorticity. The thickness of the rotational boundary layer will therefore depend on the speed of injection. Throughout the chamber, a linear correlation, given by Eq. (97), prescribes the depth of penetration and the penetration number. Unlike the axially dominated wave problem for which the wall-normal depth of penetration y_p reaches a maximum inviscid limit as $S_p \to \infty$, the axial depth of penetration, z_p, continues to grow linearly with S_p up to the point where M_b would have exceeded the upper injection threshold of the model $\left(\text{i.e. } M_b \le 0.3\right)$.

D. Wave Properties

In addition to the penetration depth, three properties will be investigated to complete the characterization of the vorticoacoustic wave behavior. These consist of the spatial wavelength, λ, the unsteady velocity overshoot factor, OF, and its spatial locus, z_{OS}. Given that the radial and tangential components have similar expressions, the following analysis is performed using the radial component only. Nonetheless, the forthcoming procedure will be equally applicable to both directional waves.

1. Spatial Wavelength

The spatial wavelength, λ_w, denotes the distance traveled by a wave during one period. It is also referred to as the distance between two consecutive peaks. To calculate λ_w, the wave propagation speed in the axial direction must be determined. To this end, the radial component of the vortical wave in Eq. (76) can be rewritten as

$$\tilde{u}_r = G(r,\theta,z)\exp\left[i\left(\frac{S}{F}z - k_{mn}t\right)\right] \tag{98}$$

where G represents the amplitude of the wave. With wave propagation in the axial direction being our primary concern, differentiation of the axial component will be essential to retrieve the corresponding velocity. The argument of Eq. (98) returns

$$\frac{S}{F}\mathrm{d}z - k_{mn}\mathrm{d}t = 0 \tag{99}$$

whence

$$V_w = \frac{\mathrm{d}z}{\mathrm{d}t} = \frac{k_{mn}F}{S} = M_b F \tag{100}$$

Knowing that the dimensionless period of oscillation is $\tau = 2\pi / k_{mn}$, the spatial wavelength becomes

$$\lambda_w = V_w \tau = \frac{2\pi}{k_{mn}}\frac{k_{mn}F}{S} = \frac{2\pi F}{S} \tag{101}$$

or, in dimensional form,

$$\lambda_w^* = \frac{2\pi F}{k_{mn}}\frac{U_b}{a_0}R \tag{102}$$

The dimensionless result is analogous to that obtained in the SRM configuration wherein longitudinal oscillations are characterized by $\lambda_w = 2\pi|V|/S$, with V representing the wall-normal injection velocity.[4,5] Consistent with classic theory of periodic flows, the velocity of propagation appears to be solely dependent on the medium and conditions, i.e. the injection Mach number and the radial distance from the centerline. However, λ_w may be affected by the transverse mode number, which is embedded in the Strouhal number. Higher modes reduce the peak-to-peak distance between oscillations, as one would expect. Another important characteristic of the generalized model lies in the connection between all properties and the injection profile F: this function controls the radial distribution of the mean flow velocity. Accordingly, oscillations in the vicinity of the sidewall propagate at a much slower rate than those located near the chamber core.

2. Unsteady Velocity Overshoot

The emergence of the Strouhal number in the argument of the vortical solution serves to control the phase difference between the strictly acoustic and vortical waves. Given their phase relations, the two waves will periodically couple, when they happen to occur at nearly the same phase, thus resulting in an overshoot of the total unsteady velocity. This amplification can reach, in many cases, twice the acoustic wave amplitude. A similar mechanism was first reported by Richardson[35] who realized that maximum velocities in reciprocating flows occurred in the vicinity of the sidewall, rather than the centerline of his resonator tubes. In order to identify the location of Richarson's overshoot, Eq. (76) must be rewritten in term of the Strouhal and penetration numbers, specifically

$$u_r' = G(t,r,\theta)\left[1 - \exp\left(i\frac{S}{F}z\right)\exp\left(-\frac{z}{S_p F^2}\right)\right] \tag{103}$$

Knowing that the overshoot takes place when both waves merge in phase, an equivalent mathematical condition may be written as $\exp(iS z_{\mathrm{OS}}/F) = -1$ in Eq. (98). The locus of the first and most pronounced overshoot can therefore be deduced asymptotically as

$$z_{\mathrm{OS}} = \frac{\pi F}{S} \tag{104}$$

In view of our underlying normalization, the induced overshoot factor can be determined by superimposing the axial contribution of the vortical correction and that of the acoustic wave. In this vein, the overshoot factor OF may be extracted from Eq. (103) by evaluating the amplitude of the vorticoacoustic velocity at $z = z_{\mathrm{OS}}$ directly from Eq. (104):

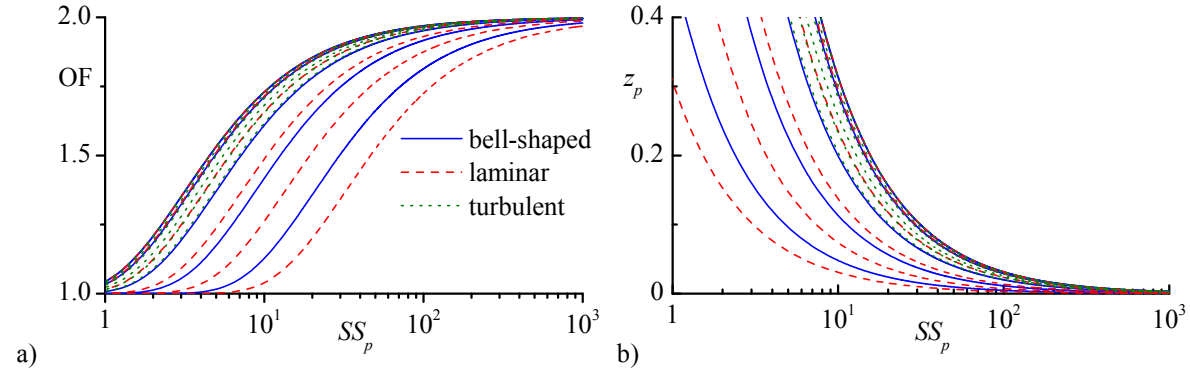

Figure 8. Effects of radial distance on a) the wave overshoot and b) its locus for the bell-shaped, laminar, and turbulent cases.

$$\mathrm{OF} = 1 + \exp\left(-\frac{\pi}{F}\frac{1}{S\,S_p}\right) = 1 + \exp\left(-\frac{\pi}{F}\frac{S}{Re_b}\right) \tag{105}$$

Figure 8a quantifies the overshoot factor and its locus for different control parameters: the Strouhal number, the penetration number, and the distance from the centerline. Figure 8a shows that the strength of the overshoot decreases as we move away from the chamber centerline and increases at higher values of $SS_p = (U_b / \sqrt{\omega_{mn} \nu_0})^2$, i.e. with larger injection velocities or smaller frequencies. However, the locus of the overshoot depends solely on the Strouhal number and the distance from the centerline. For all physical values of the Strouhal number, the overshoot takes place in the neighborhood of the headwall, in a segment that stretches over less than 25 percent of the chamber radius.

Recalling that faceplate injectors protrude inwardly, it is clear that they can be subject to oscillations reaching twice the strength of the predicted acoustic waves, even in the linear range. Additionally, it appears that the distance from the centerline affects the overshoot and its properties. The slower injection rate near the sidewalls leads to a smaller overshoot factor. As one may infer from Eq. (104) and Fig. 8b, z_{OS} decreases while moving away from the centerline to the extent of vanishing along the sidewall. This behavior shifts the line of maximum wave amplitude closer to the headwall as $r \to 1$. In the case of a liquid rocket engine, these spatial excursions of peak transverse amplitudes serve to amplify shearing stresses on the injectors, where coupling between modes, reflections, and standing wave motion can lead to further steepening and shock-like behavior.

V. Standing Wave Formulation

A. Traveling vs. Standing Wave Basics

For the reader's convenience, we begin this section with a basic overview. It is well known, for example, that a traveling wave exhibits nodes and extrema that move in the direction of propagation.[36] In elemental form, sinusoidal planar waves traveling in the positive and negative z-directions can be written as

Right-traveling: $$u(z,t) = A\sin(kz - \omega t) \tag{106}$$

Left-traveling: $$u(z,t) = A\sin(-kz - \omega t) \tag{107}$$

where A denotes their amplitude.

On the other hand, a standing wave is produced when two waves with the same frequency, wavelength, and amplitude merge together while traveling in opposite directions. The resulting nodes and extrema become stationary within the medium, hence the term standing.[36] The resulting wave can be synthesized from the sum of the two traveling waves,

$$u_S(z,t) = A\sin(kz - \omega t) + A\sin(-kz - \omega t) = 2A\sin(-\omega t)\cos(kz) \tag{108}$$

The linear superposition of traveling or standing waves forms wave packets. These groups of waves are characterized by a group velocity that represents the propagation speed of the packet in a medium. The group velocity is defined as:

$$V_G \equiv \frac{\partial \omega}{\partial k} \tag{109}$$

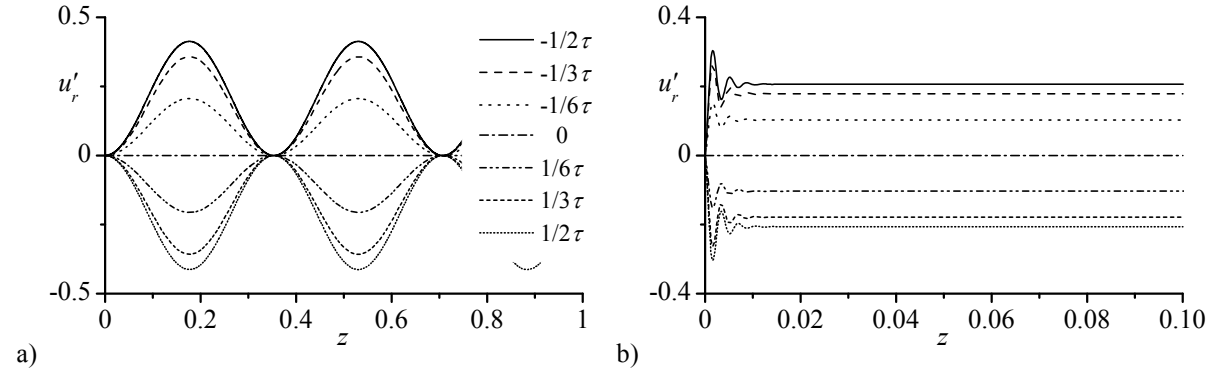

Figure 9. Vorticoacoustic radial velocity for standing waves at inlet Mach numbers corresponding to a) 0.3 and b) 0.003.

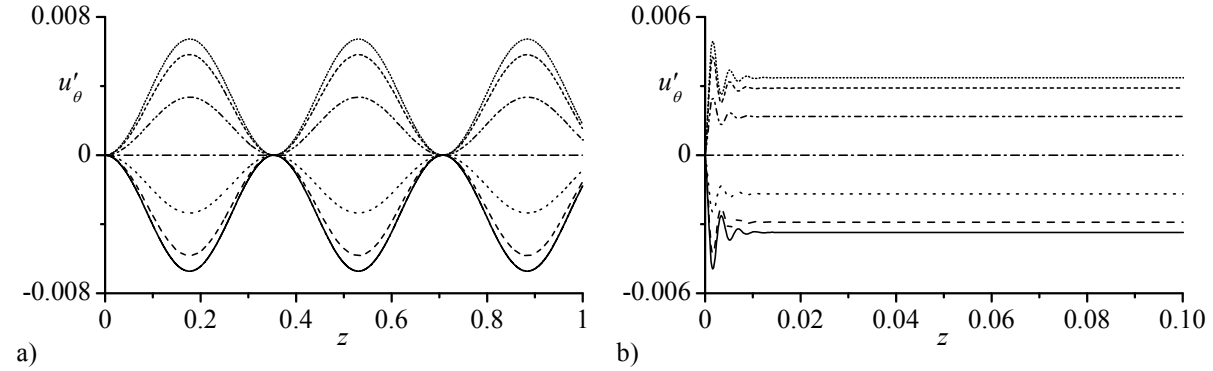

Figure 10. Vorticoacoustic tangential velocity for standing waves at inlet Mach numbers corresponding to a) 0.3 and b) 0.003.

where ω denotes the wave's angular frequency and k, the angular wavenumber. The propagation velocity of a single wave is known as 'phase velocity.' In addition to linear superposition, it is possible to superimpose different waves nonlinearly.

B. Standing Vorticoacoustic Wave

As per Eq. (98), our vortical wave model leads to a right-traveling wave. However, when the flow is choked at the nozzle, the chamber's exit section may act as a solid boundary that causes the wave to rebound.[37] The left-traveling reflected wave exhibits the form

$$\tilde{u}_r = G(r,\theta,z)\exp\left[i\left(-\frac{S}{F}z - k_{mn}t\right)\right] \tag{110}$$

The summation of Eqs. (98) and (110) produces the standing radial wave representation:

$$\tilde{u}_r = 2G(r,\theta,z)e^{-ik_{mn}t}\cos\left(\frac{S}{F}z\right) \tag{111}$$

In our problem, this expression becomes

$$\tilde{u}_r = \frac{2A_r i}{k_{mn}\gamma}e^{-ik_{mn}t}J'_m(k_{mn}r)\cos(m\theta)\cos\left(\frac{S}{F}z\right)\exp\left(-\frac{z}{S_pF^2}\right) \tag{112}$$

where A_r is the integration constant first introduced in Eq. (51). To ensure the satisfaction of the no-slip requirement at the headwall, $u'(z=0)=0$, it can be shown that A_r must be set equal to $-1/2$. The ensuing standing wave in the radial direction turns into

$$u'_r = \frac{i}{k_{mn}\gamma}e^{-ik_{mn}t}J'_m(k_{mn}r)\cos(m\theta)\left[1-\cos\left(\frac{S}{F}z\right)\exp\left(-\frac{z}{S_pF^2}\right)\right] \tag{113}$$

and, in the tangential direction, into

$$u'_\theta = \frac{i}{k_{mn}\gamma}\frac{m}{r}e^{-ik_{mn}t}J_m\left(k_{mn}r\right)\sin\left(m\theta\right)\left[1-\cos\left(\frac{S}{F}z\right)\exp\left(-\frac{z}{S_pF^2}\right)\right] \tag{114}$$

It should be noted that the axial velocity fluctuation is not presented above because: a) it represents a negligible contribution, being an order smaller than u'_r or u'_θ, and b) it leads to a rather long and laborious expression relative to Eqs. (113) and (114).

Figure 10 displays the mode shapes of the radial and tangential disturbances corresponding to the standing wave structure along the axis of the chamber at varying times. To be consistent with the traveling wave plots, results are depicted for $\delta = 0.000647, r = 1/\sqrt{2}, \theta = \frac{1}{4}\pi, M_b = \left(0.003, 0.3\right)$, and the first tangential/radial modes using k_{11}. The graphs in Fig. 10 span over half a cycle, thus illustrating the behavior of the standing wave with respect to time. The most striking outcome may be connected with the maximum value of the standing wave when compared to its traveling counterpart. For all cases considered, the standing waves exhibit peaks that are twice as large as those of their traveling wave components. This magnification points to the importance of accounting for the reflected wave contributions in a simulated LRE enclosure.

VI. Conclusions

In our efforts to mimic the cold flow environment in a simple liquid rocket engine, asymptotic expansion tools are used to capture small-to-moderate amplitude oscillations that are dominated by their transverse motion in a short circular cylinder. A generalized formulation is advanced and tested for uniform, bell-shaped, laminar, and turbulent injection profiles at the chamber headwall. After decomposing the unsteady wave into potential and rotational fields, the latter is resolved using a boundary layer formulation that relies on a small viscous parameter, δ. This parameter corresponds to the square root of the inverted acoustic Reynolds number based on viscosity and the speed of sound. At the outset, several fundamental flow features are unraveled including the radial, tangential, and axial velocities of the time-dependent vortical field. The pseudo-pressure associated with the rotational motion is also determined rigorously and shown to be immaterial to the present analysis.

Our generic solution is verified by comparing its results to those obtained previously assuming uniform[1] or bell-shaped injection configurations.[2] These special cases are recovered identically. The uniform injection model, however, leads to a transverse wave solution that permits slippage along the sidewall. An improved formulation is herein produced that gives rise to a more suitable representation of the oscillatory field. The latter is shown to satisfy the no-slip requirement at both headwall and chamber sidewall for the radial and axial components. It is hoped that this mathematical strategy can be further refined and extended to target higher-order models of three-dimensional traveling and standing waves in various geometric settings.

Moreover, two parameters, the penetration and Strouhal numbers, are identified as controlling factors of the wave's axial propagation. The latter's dependence on these keystone parameters is ascertained to be nearly identical to its counterpart arising in the longitudinal wave analog encountered in the treatment of unsteady SRM flows.[5,6] The advent of these parameters enables the full characterization of the penetration depth in the direction normal to the injecting surface. With the vorticoacoustic solution in hand, fundamental wave propagation properties are carefully extracted and discussed. These include the depth of penetration and Richardson's overshoot factor associated with transverse waves. These are found to be strongly dependent on the Strouhal and penetration numbers.

Lastly, the locus of peak wave amplitudes, where Richardson's overshoot occurs, is determined to be within a quarter radius, thus placing the maximum shearing stresses resulting from transverse wave oscillations in the close vicinity of the headwall. Despite the linear restrictions of this work, our findings indicate that the merging of vortical and acoustic wave modes doubles the amplitude of the acoustic wave in the region of protruding injectors, for a large range of frequencies and injection Mach numbers. Moreover, by considering the presence of wave reflections, the structure of the emerging standing waves is shown to exhibit amplitudes that are twice as large as their traveling wave constituents. We conclude that, irrespective of whether the chamber is dominated by traveling or standing wave motions, and notwithstanding the possibility of nonlinear mode coupling and its wave steepening tendency, a doubling of acoustic velocity amplitudes may be expected in the headwall region. These observations may be viewed as crucially relevant to our understanding of wave propagation in thrust chambers and to the load ratings and reciprocating stresses that such oscillatory motions stand to generate.

Acknowledgments

This material is based on work supported partly by the National Science Foundation and partly by the University of Tennessee Space Institute, through institutional cost sharing.

References

[1]Fischbach, S., Flandro, G., and Majdalani, J., "Acoustic Streaming in Simplified Liquid Rocket Engines with Transverse Mode Oscillations," *Physics of Fluids,* Vol. 22, No. 6, 2010, pp. 063602-21. doi: 10.1063/1.3407663

[2]Haddad, C. T., and Majdalani, J., "Transverse Waves in Simulated Liquid Rocket Engines," AIAA Paper 2011-6029, July-August 2011.

[3]Jankowski, T., and Majdalani, J., "Vortical and Acoustical Mode Coupling inside a Porous Tube with Uniform Wall Suction," *Journal of the Acoustical Society of America,* Vol. 117, No. 6, 2005, pp. 3448-3458. doi: 10.1121/1.1905639

[4]Majdalani, J., and Flandro, G., "The Oscillatory Pipe Flow with Arbitrary Wall Injection," *Proceedings of the Royal Society of London, Series A,* Vol. 458, No. 2023, 2002, pp. 1621-1651. doi: 10.1098/rspa.2001.0930

[5]Majdalani, J., and Roh, T., "The Oscillatory Channel Flow with Large Wall Injection," *Proceedings of the Royal Society of London, Series A,* Vol. 456, No. 1999, 2000, pp. 1625-1657. doi: 10.1098/rspa.2000.0579

[6]Majdalani, J., "Multiple Asymptotic Solutions for Axially Travelling Waves in Porous Channels," *Journal of Fluid Mechanics,* Vol. 636, No. 1, 2009, pp. 59-89. doi: 10.1017/S0022112009007939

[7]Majdalani, J., and Rienstra, S., "Two Asymptotic Forms of the Rotational Solution for Wave Propagation inside Viscous Channels with Transpiring Walls," *Quarterly Journal of Mechanics and Applied Mathematics,* Vol. 55, No. 1, 2002, pp. 141-162. doi: 10.1093/qjmam/55.1.141

[8]Fischbach, S., Majdalani, J., and Flandro, G., "Acoustic Instability of the Slab Rocket Motor," *Journal of Propulsion and Power,* Vol. 23, No. 1, 2007, pp. 146-157. doi: 10.2514/1.14794

[9]Maslen, S., and Moore, F., "On Strong Transverse Waves without Shocks in a Circular Cylinder," *Journal of the Aeronautical Sciences,* Vol. 23, No. 6, 1956, pp. 583-593.

[10]Arfken, G., "Mathematical Methods for Physicists," Academic Press, Orlando, FL, 1985, pp. 492-493.

[11]Forsythe, G. E., Malcolm, M. A., and Moler, C. B., *Computer Methods for Mathematical Computations*, Prentice Hall Professional Technical Reference, 1977, p. 259.

[12]Flandro, G. A., Majdalani, J., and Sims, J. D., "Nonlinear Longitudinal Mode Instability in Liquid Propellant Rocket Engine Preburners," AIAA Paper 2004-4162, July 2004.

[13]Flandro, G. A., Majdalani, J., and Sims, J. D., "On Nonlinear Combustion Instability in Liquid Propellant Rocket Engines," AIAA Paper 2004-3516, July 2004.

[14]Renie, J. S., Lilley, J. S., and Frederick, R. A., "Aluminum Particle Combustion in Composite Solid Propellants," AIAA Paper 1982-1110, June 1982.

[15]Chu, B.-T., and Kovásznay, L. S. G., "Non-Linear Interactions in a Viscous Heat-Conducting Compressible Gas," *Journal of Fluid Mechanics,* Vol. 3, No. 5, 1958, pp. 494-514. doi: 10.1017/S0022112058000148

[16]Zhao, Q., Staab, P., Kassoy, D., and Kirkköprü, K., "Acoustically Generated Vorticity in an Internal Flow," *Journal of Fluid Mechanics,* Vol. 413, No. 1, 2000, pp. 247-285. doi: 10.1017/S0022112000008454

[17]Criminale, W., Jackson, T., Lasseigne, D., and Joslin, R., "Perturbation Dynamics in Viscous Channel Flows," *Journal of Fluid Mechanics,* Vol. 339, No. 1, 1997, pp. 55-75. doi: 10.1017/S0022112097005235

[18]Anderson, J. D., *Modern Compressible Flow with Historical Perspective*, 3rd ed., McGraw-Hill, New York, 2003.

[19]Saad, T., Maicke, B. A., and Majdalani, J., "Coordinate Independent Forms of the Compressible Potential Flow Equations," AIAA Paper 2011-5862, July-August 2011.

[20]Maicke, B. A., Saad, T., and Majdalani, J., "On the Compressible Hart-McClure Mean Flow Motion in Simulated Rocket Motors," AIAA Paper 2010-7077, July 2010.

[21]Majdalani, J., and Van Moorhem, W., "Multiple-Scales Solution to the Acoustic Boundary Layer in Solid Rocket Motors," *Journal of Propulsion and Power,* Vol. 13, No. 2, 1997, pp. 186-193. doi: 10.2514/2.5168

[22]Sutton, G. P., and Biblarz, O., *Rocket Propulsion Elements*, John Wiley, New York, 2001.

[23]Berman, A. S., "Laminar Flow in Channels with Porous Walls," *Journal of Applied Physics*, Vol. 24, No. 9, 1953, pp. 1232-1235. doi: 10.1063/1.1721476

[24]Culick, F., "Rotational Axisymmetric Mean Flow and Damping of Acoustic Waves in a Solid Propellant Rocket," *AIAA Journal*, Vol. 4, No. 8, 1966, pp. 1462-1464. doi: 10.2514/3.3709

[25]Brown, R. S., Blackner, A. M., Willoughby, P. G., and Dunlap, R., "Coupling between Acoustic Velocity Oscillations and Solid Propellant Combustion," *Journal of Propulsion and Power*, Vol. 2, No. 5, 1986, pp. 428-437. doi: 10.2514/3.22925

[26]Proudman, I., "An Example of Steady Laminar Flow at Large Reynolds Number," *Journal of Fluid Mechanics*, Vol. 9, No. 4, 1960, pp. 593-602. doi: 10.1017/S002211206000133X

[27]Beddini, R. A., "Injection-Induced Flows in Porous-Walled Ducts," *AIAA Journal*, Vol. 24, No. 11, 1986, pp. 1766-1773. doi: 10.2514/3.9522

[28]Chedevergne, F., Casalis, G., and Féraille, T., "Biglobal Linear Stability Analysis of the Flow Induced by Wall Injection," *Physics of Fluids*, Vol. 18, No. 1, 2006, pp. 014103-14. doi: 10.1063/1.2160524

[29]Griffond, J., and Casalis, G., "On the Nonparallel Stability of the Injection Induced Two-Dimensional Taylor Flow," *Physics of Fluids*, Vol. 13, No. 6, 2001, pp. 1635-1644. doi: 10.1063/1.1367869

[30]Majdalani, J., and Saad, T., "The Taylor-Culick Profile with Arbitrary Headwall Injection," *Physics of Fluids*, Vol. 19, No. 9, 2007, pp. 093601-10. doi: 10.1063/1.2746003

[31]Majdalani, J., "Analytical Models for Hybrid Rockets," *Fundamentals of Hybrid Rocket Combustion and Propulsion*, edited by K. Kuo and M. J. Chiaverini, AIAA Progress in Astronautics and Aeronautics, Washington, DC, 2007, pp. 207-246.

[32]Horton, M. D., and McGie, M. R., "Participate Damping of Oscillatory Combustion," *AIAA Journal*, Vol. 1, No. 6, 1963, pp. 1319-1326. doi: 10.2514/3.1787

[33]Carrier, B. T., and Carlson, F. D., "On the Propagation of Small Disturbances in a Moving Compressible Fluid," *Quarterly of Applied Mathematics*, Vol. 4, No. 1, 1946, pp. 1-12.

[34]Majdalani, J., "The Boundary Layer Structure in Cylindrical Rocket Motors," *AIAA Journal*, Vol. 37, No. 4, 1999, pp. 505-508. doi: 10.2514/2.742

[35]Richardson, E., "The Amplitude of Sound Waves in Resonators," *Proceedings of the Physical Society, London*, Vol. 40, No. 27, 1928, pp. 206-220. doi: 10.1088/0959-5309/40/1/328

[36]Price, E. W., "Experimental Solid Rocket Combustion Instability," *Proceedings of the Combustion Institute.*, Vol. 10, No. 1, 1965, pp. 1067-1082. doi: 10.1016/S0082-0784(65)80247-8

[37]Fischbach, S. R., "Streaming Effects in Liquid Injection Rocket Engines with Transverse Mode Oscillations," Ph.D. Dissertation, University of Tennessee, 2007.